

## RESEARCH ARTICLE

10.1029/2017JB015131

## Key Points:

- The tomographic model resolves two elongated magma reservoirs and a subsiding trapdoor caldera
- Excess magma supply from the Cobb hot spot plume causes Axial Seamount to behave like a fast spreading ridge
- The improved relocation of the local seismicity resolves a network of conjugate outward and inward dipping faults beneath the caldera walls

## Supporting Information:

- Supporting Information S1

## Correspondence to:

A. F. Arnulf,  
aarnulf@ig.utexas.edu

## Citation:

Arnulf, A. F., Harding, A. J., Kent, G. M., & Wilcock, W. S. D. (2018). Structure, seismicity, and accretionary processes at the hot spot-influenced Axial Seamount on the Juan de Fuca Ridge. *Journal of Geophysical Research: Solid Earth*, 123, 4618–4646. <https://doi.org/10.1029/2017JB015131>

Received 26 OCT 2017

Accepted 1 JUN 2018

Accepted article online 9 JUN 2018

Published online 29 JUN 2018

©2018. The Authors.

This is an open access article under the terms of the Creative Commons Attribution-NonCommercial-NoDerivs License, which permits use and distribution in any medium, provided the original work is properly cited, the use is non-commercial and no modifications or adaptations are made.

## Structure, Seismicity, and Accretionary Processes at the Hot Spot-Influenced Axial Seamount on the Juan de Fuca Ridge

 A. F. Arnulf<sup>1</sup> , A. J. Harding<sup>2</sup> , G. M. Kent<sup>3</sup>, and W. S. D. Wilcock<sup>4</sup> 

<sup>1</sup>Institute for Geophysics, Jackson School of Geosciences, University of Texas at Austin, Austin, TX, USA, <sup>2</sup>Cecil H. and Ida M. Green Institute of Geophysics and Planetary Physics, Scripps Institution of Oceanography, University of California, San Diego, La Jolla, CA, USA, <sup>3</sup>Nevada Seismological Laboratory, University of Nevada, Reno, Reno, NV, USA, <sup>4</sup>School of Oceanography, University of Washington, Seattle, WA, USA

**Abstract** Axial Seamount is the most volcanically active site of the northeast Pacific, and it has been monitored with a growing set of observations and sensors during the last two decades. Accurate imaging of the internal structure of volcanic systems is critical to better understand magma storage processes and to quantify mass and energy transport mechanisms in the crust. To improve the three-dimensional velocity structure of Axial Seamount, we combined 469,891 new traveltimes arrivals, from 12 downward extrapolated seismic profiles, with 3,962 existing ocean-bottom-seismometers traveltimes arrivals, into a joint tomographic inversion. Our approach reveals two elongated magma reservoirs, with melt fraction up to 65%, representing an unusually large volume of melt (26–60 km<sup>3</sup>), which is likely the result of enhanced magma supply from the juxtaposition of the Cobb hot spot plume (0.26–0.53 m<sup>3</sup>/s) and the Axial spreading segment (0.79–1.06 m<sup>3</sup>/s). The tomographic model also resolves a subsided caldera floor that provides an effective trap for ponding lava flows, via a “trapdoor” mechanism. Our model also shows that Axial’s extrusive section is thinnest beneath the elevated volcano, where anomalously thick (11 km) oceanic crust is present. We therefore suggest that focused and enhanced melt supply predominantly thickens the crust beneath Axial Seamount through dike accretion and gabbro crystallization. Lastly, we demonstrate that our three-dimensional velocity model provides a more realistic starting point for relocating the local seismicity, better resolving a network of conjugate outward and inward dipping faults beneath the caldera walls.

### 1. Introduction

Separation of oceanic plates along the 65,000-km-long mid-ocean ridge (MOR) spreading system pulls mantle upward and induces decompression melting accounting for ~75% of Earth’s magmatic budget, producing ~21 km<sup>3</sup> of magma each year (Crisp, 1984). Beneath MORs, the rate of magma supply strongly determines the thermal structure of the oceanic crust, which, in turn, influences rheology, crystallization, tectonic processes, ridge morphology, and hydrothermal circulation (Coogan, 2014). Spreading rate is a dominant factor controlling the rate of magma supply at MORs; therefore, it is a critical variable in models for the formation and structure of the oceanic crust (e.g., Chen & Lin, 2004; Phipps Morgan & Chen, 1993; Purdy et al., 1992; Sinton & Detrick, 1992; Sleep, 1975). Nevertheless, other parameters controlling magma supply exist, including mantle temperature and composition, or magma focusing in both space and time (e.g., at segment centers). There is a wide range of spreading rates for the global MOR system, forming three main categories: slow (<40 mm/year), intermediate (40 to 80 mm/year) and fast (>80 mm/year) spreading ridges. Axial magma chambers (AMC) are generally steady state and well-imaged features at intermediate and fast spreading ridges (e.g., Blacic et al., 2004; Carbotte et al., 2008; Harding et al., 1989; Kent et al., 2000) but often absent (e.g., Detrick et al., 1990) or short-lived, small, and deep features at slow spreading ridges (e.g., Calvert, 1995; Singh et al., 2006). Additionally, there is a general shoaling of the AMC horizon with increasing spreading rate, with the most significant depth variations observed at intermediate rates.

On the other hand, hot spots are generally thought to arise from buoyant upwelling of anomalously hot convection plumes originating in the deep mantle (Morgan, 1971) and produce 2–4 km<sup>3</sup> of magma each year worldwide (Crisp, 1984). Among the ~50 identified present-day hot spots, ~20 appear to be interacting with the MOR system (Ito et al., 2003), resulting in altered magmatic, geochemical, and hydrothermal systems. On the intermediate spreading Juan de Fuca Ridge (JdFR), Axial Seamount is the most volcanically active site in

the northeast Pacific due to the merging of the JdFR and Cobb hot spot magmatic systems. Axial Seamount has been monitored through two eruption cycles with an increasing number of seafloor instruments, culminating in the deployment of a long-term, real-time, wired-to-shore, seafloor observatory in 2014 (Kelley et al., 2014). Axial Seamount is therefore an ideal site to study MOR-plume interaction processes and evaluate the influence of excess magma supply onto rheological, volcanic, tectonic, and hydrothermal processes.

Seismic imaging of subsurface magmatic systems is critical to our understanding of melt storage and melt migration in active volcanoes, yet high-resolution tomographic imaging of magma bodies has remained difficult, mainly because of the combination of incomplete spatial data coverage and the assumptions underpinning ray-based tomography (Lees, 2007). On land, obtaining good coverage with active source seismology is challenging because of the often complex terrain and the high cost of experiments (e.g., Beachly et al., 2012; Heath et al., 2015; Zandomenighi et al., 2013). In the oceans, obtaining dense, evenly distributed, wide-angle, wide-azimuth, and broadband frequency controlled-source data is achievable with modern marine seismic acquisition methods and so high-resolution imaging of magma bodies is at least theoretically within the community's reach (e.g., Arnulf, Harding, Kent, Carbotte, et al., 2014; Kent et al., 2000; Paulatto et al., 2012).

Historically, three-dimensional (3-D) marine tomographic investigations of mid-ocean spreading centers have relied solely on sparsely instrumented arrays of ocean bottom seismographs (OBSs; e.g., Dunn et al., 2000; Seher et al., 2010; Toomey et al., 1990; West et al., 2001). Even today, the spacing of OBSs is often on the order of 5 km or more, and tomographic models are strongly smoothed to compensate for the inadequate horizontal sampling of structures by crossing raypaths.

Streamer tomography using surface multichannel (MCS) data is an alternative to OBS tomography that can improve the horizontal sampling of crustal structures by providing source and receiver spacings of tens of meters (Canales et al., 2008; Zelt et al., 2004). However, because both the source and receiver are now located at the sea surface, far from the seafloor, critical velocity information carried by refracted arrivals is typically masked behind strong scattered energy from the seafloor, preventing a tomographic approach. Fortunately, Arnulf et al. (2011) and Arnulf, Harding, Kent, Singh, et al. (2014) showed that by using a downward continuation methodology both source and receiver wavefields from the MCS data can be propagated down to the seafloor, simulating a Synthetic Ocean Bottom Experiment (SOBE). In a SOBE deployment, crustal refracted arrivals become first arrivals that can be used for tomographic imaging. This approach has been used to study the crustal structure beneath several MORs (Arnulf, Harding, Kent, Carbotte, et al., 2014; Arnulf et al., 2011; Harding et al., 2016; Henig et al., 2012; Marjanovic et al., 2017). However, because of the limited streamer lengths ( $\leq 6$  km) available for those studies, the refraction arrivals sampled only the upper 1–1.5 km of crust. With a 15-km-long state-of-the-art streamer, over 4 km of crust below the seafloor (bsf) can be accurately sampled. Ghosal et al. (2014) demonstrated this for the northwest Sumatra subduction system using industry data, while more recently Kardell et al. (2016) obtained similar coverage of the oceanic crust using academic data collected by the R/V Langseth.

In this study, we use historical seismic data sets to generate a high-resolution 3-D tomographic image of the magmatic systems beneath Axial Seamount. The MCS data set at this location were collected with a 6-km-long streamer (Carbotte et al., 2008) again limiting refractions to the upper 1–1.5 km. Since the magmatic system extends below this depth, we combine traveltimes extracted from the MCS data using the SOBE method with traveltimes from an earlier OBS experiment (West et al., 2001). We also include a priori geometrical constraints on the shape of the main magma reservoir (MMR) obtained from existing high-quality depth-migrated images obtained from the MCS data (Arnulf, Harding, Kent, Carbotte, et al., 2014).

This paper provides a more complete view of the upper crustal structure of Axial Seamount than the earlier investigations of West et al. (2001) and Arnulf, Harding, Kent, Carbotte, et al. (2014). We use these new results to characterize the distribution, geometry, and melt content of the magmatic system, from which we infer the relative importance of the Cobb hot spot plume and JdFR in terms of crustal production rate and magma volumetric flux. We investigate the effect of enhanced and localized magma volumetric flux on the characteristics of the MMR. Additionally, we examine the distribution and thickness of extrusives over the volcano, which is used to understand accretionary processes. Finally, this paper uses the new 3-D tomographic velocity structure to obtain improved local earthquakes hypocentral locations to understand caldera dynamics.

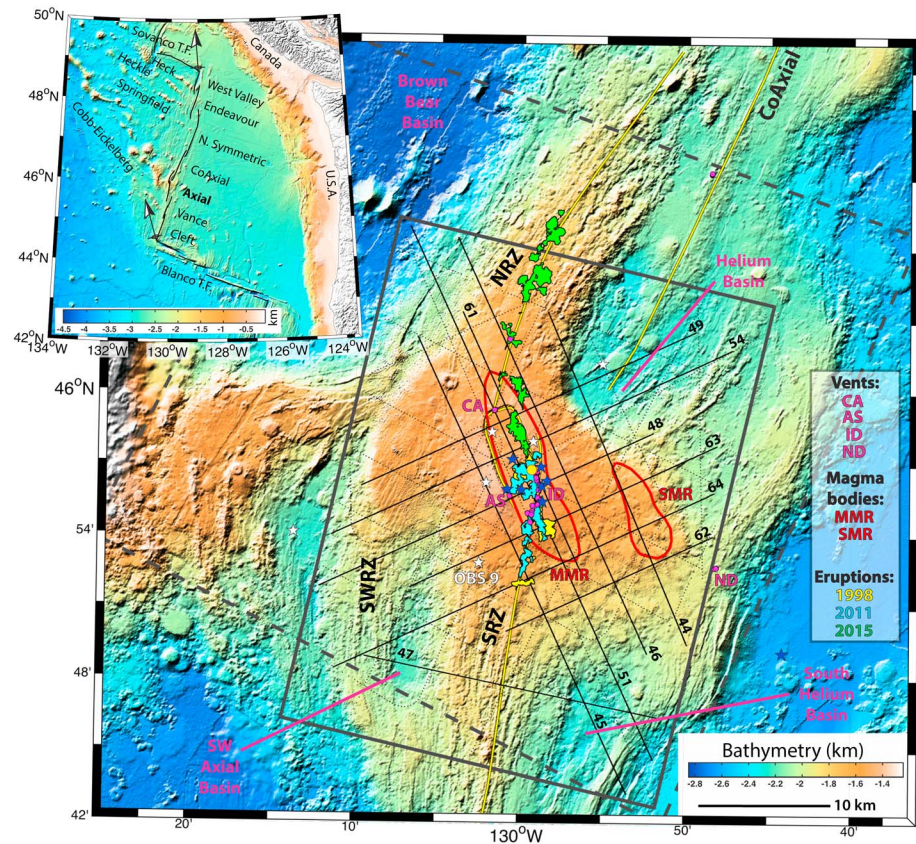


**Figure 1.** Shaded bathymetric map of Axial Seamount on the JdFR. The thick dashed gray rectangle marks the outline of the OBS-tomographic volume of West et al. (2001, 2003). The thick solid gray rectangle marks the outline of our new 3-D tomographic volume, centered on  $45.91792^{\circ}\text{N}/-129.99305^{\circ}\text{W}$  and rotated  $12.9^{\circ}\text{N}$ . We combined traveltimes picks from 12 downward extrapolated seismic lines (solid thin black lines labeled with line number), with all seismic shots (thin dotted lines) to five OBSs (white stars) from the West et al. (2001, 2003) experiment, into a joint tomographic inversion. OBS 9 from the West et al. (2001, 2003) survey is presented in Figure 3 and labeled in white. The red contours are the outlines of the main and secondary magma reservoir (MMR and SMR). The yellow lines mark spreading center axes and outline the U-shaped caldera. The colored areas mark the extent of the 1998, 2011, and 2015 eruption flows (data are from Clague et al., 2018a, 2018b). The yellow circle denotes the centroid of the prolate-spheroid deformation model from the 2015 eruption (Nooner & Chadwick, 2016). The magenta dots are hydrothermal vents from the four recognized fields (ID: International District, AS: Ashes, CA: Casm, and ND: New Dymond). The blue stars mark the locations of OOI's seismometers. NRZ, SRZ, and SWRZ are the north, south, and southwest rift zones. Inset map shows the location of Axial spreading segment relative to other segments of the JdFR.

## 2. Background

### 2.1. Regional Setting

The JdFR is a 480-km-long series of intermediate-rate spreading centers (56 mm/a; Wilson, 1993), located  $\sim 400$  km off the coast of northwestern United States and Canada between  $44^{\circ}20'\text{N}$  and  $48^{\circ}50'\text{N}$  (Figure 1). The JdFR extends from the Sovanco transform fault in the north to the Blanco transform fault in the south and comprises seven spreading segments: West Valley, Endeavor, Northern Symmetric, Coaxial, Axial, Vance, and Cleft. The entire ridge system is migrating to the northwest relative to the absolute reference frame at an angle and rate that varies from  $-32^{\circ}\text{N}$  and 32 mm/a at its southern end to  $-21^{\circ}\text{N}$  and 28 mm/a at its northern end (Small & Danyushevsky, 2003).

The west flank of the JdFR is characterized by several seamount chains oriented approximately to the northwest (Delaney et al., 1981; Desonie & Duncan, 1990; Karsten & Delaney, 1989). The most prominent one, known as the Cobb-Eickelberg seamount chain, is a 1,800-km long discontinuous trail of seamounts extending from the  $\sim 30$ -Ma-old Patton-Murray seamounts all the way to the JdFR.

Axial Seamount on the JdFR is the most recent seamount from the Cobb-Eickelberg seamount chain, and it is the current locus of volcanic activity associated with the Cobb hot spot (Figure 1). Axial Seamount, located at 46°N, 130°W, is the most prominent and shallowest feature (summit at <1,500 m depth) of the JdFR. Early bathymetric and side scan sonar surveys (Embley et al., 1990; Johnson & Embley, 1990) revealed a wide (15–25 km in diameter), dome-shaped volcano rising ~700 m above the adjacent ridge axis. The summit of the volcano hosts an 8.6-km-long, 3.3-km-wide, horseshoe-shaped caldera that opens to the southeast, where hydrothermal vent communities are located adjacent to recent volcanic flows (Caress et al., 2012; Chadwick et al., 2013; Embley et al., 1990). Two ~50-km-long major rift zones extend from the summit caldera to the north and south and overlap the neighboring Vance and Coaxial ridge segments over more than 30 km (labeled south and north rift zones: SRZ and NRZ in Figure 1).

## 2.2. Geophysical Studies

Axial Seamount is one of the best-studied volcanoes on the global MOR system, and its structure and activity have been investigated for over three decades. It became the site of National Oceanic and Atmospheric Administration's NeMO (New Millennium Observatory) seafloor observatory shortly before the 1998 eruption, and since 2014, it has been a site on the Cabled Array, real-time observatory that is part of National Science Foundation's Ocean Observatories Initiative (OOI; Kelley et al., 2014).

Analysis of magnetic and bathymetric data suggests that volcanic activity at Axial segment initiated within the Brunhes anomaly at ~0.5 Ma with a 20-km westward jump of the ridge to override the Cobb hot spot (Delaney et al., 1981). Using gravity data, Hooft and Detrick (1995) inferred a warmer mantle regime (+30–40 °C) and a ~30% increase in crustal production at Axial Seamount as well as 0.5–2 km of additional oceanic crustal thickness over a 100-km-long section of the ridge. A narrow (20–40 km in diameter) crustal root up to 11 km thick was later imaged beneath Axial Seamount using active seismic data (West et al., 2003). The influence of the Cobb hot spot on melt production and crustal thickness along the JdFR was confirmed by bathymetric, seismic, and geochemistry data. Chadwick et al. (2005) showed that most lava samples along the Axial segment contained between 20 and 40% of the Cobb hot spot geochemical component, with some extreme values reaching 60%, but were dominated by the mid-ocean ridge basalt (MORB) end-member. Carbotte et al. (2008) showed that an AMC reflector is present beneath only the central ~19% of the Axial segment, where the JdFR intersects with the Cobb-Eickelberg seamount chain. Using refraction data from active seismic shots to six OBSs, West et al. (2001) successfully imaged the large-scale geometry of an anomalously large (250 km<sup>3</sup>), and shallow (1.5 km bsf) crustal magma reservoir beneath the summit caldera. Later, Arnulf, Harding, Kent, Carbotte, et al. (2014) refined the image using four MCS seismic lines and wavefield-based imaging methods. They found that this complex magma reservoir has an elongated geometry and imaged a network of upper crustal fractures.

The most recent eruptions at Axial Seamount occurred in 1998, 2011, and 2015. The 1998 eruption produced lava flows along 11 km of the upper SRZ (Chadwick et al., 2013). An intense swarm of earthquakes lasted 11 days and was later linked to a diking event, which migrated all the way to the southern extremity of the SRZ, ~50 km away from the center of the summit caldera (Dziak & Fox, 1999). After years of volcanic inflation following the 1998 eruption (Chadwick et al., 2012; Nooner & Chadwick, 2009), the volcano erupted again on 6 April 2011 (Dziak et al., 2012). Near the volcano summit, the extent of the lava flows reached nearly 3 km across the caldera and 10 km in length along the upper SRZ (Caress et al., 2012; Clague et al., 2017; Figure 1); however, the thickest flows (up to 137 m) were found ~23 km south of the caldera along the SRZ. Most recently, on 24 April 2015, the OOI monitoring network captured a volcanic eruption (Caplan-Auerbach et al., 2017; Levy et al., 2018; Nooner & Chadwick, 2016; Wilcock, Tolstoy, et al., 2016; Wilcock et al., 2018). Inflation before the eruption and deflation during it was accommodated by the reactivation of an outward dipping caldera ring fault, which likely provided a pathway for a dike that propagated both southward and northward beneath the east wall of the caldera (Wilcock, Tolstoy, et al., 2016). Then, the eruption stepped westward and a dike propagated ~15 km along the NRZ (Chadwick et al., 2016; Clague et al., 2017; Wilcock, Tolstoy, et al., 2016; Figure 1). Based on bathymetric remapping data, 13 distinct flows erupted on the seafloor (Chadwick et al., 2016; Clague et al., 2017). The most mafic flows were found in the NE caldera (MgO up to 8.3%), while flows on the NRZ were gradually more evolved (MgO down to 7.1%). The northernmost three flows were up to 67–128 m thick and represented ~92% of the erupted volume (Chadwick et al., 2016; Figure 1). Additional information about these three eruptions can be found in Table 1.

**Table 1**

Maximum Caldera Deflation and Volumes of Lava Flows and Magmatic Intrusions for the Three Most Recent Eruptions at Axial Seamount (Caress et al., 2012; Chadwick et al., 1999, 2012, 2013, 2016; Clague et al., 2017; Embley et al., 1999; Fox, 1999; Nooner & Chadwick, 2009, 2016)

	Maximum Caldera deflation (m)	Volume of seafloor lava flows (km <sup>3</sup> )	Volume of magma intrusion (km <sup>3</sup> )	Total volume of magma extracted from the reservoir (km <sup>3</sup> )
1998	3.2 (Fox, 1999; Nooner & Chadwick, 2009)	0.031 (Chadwick et al., 2013; Embley et al., 1999)	0.1–0.15 (Chadwick et al., 1999)	0.131–0.181
2011	2.43 (Chadwick et al., 2012)	0.094 (Caress et al., 2012; Clague et al., 2017)	0.048	0.147 (Chadwick et al., 2012)
2015	2.45 (Nooner & Chadwick, 2016)	0.1552 (Chadwick et al., 2016; Clague et al., 2017)	0.14	0.288 (Nooner & Chadwick, 2016)

### 3. Tomography Data and Methods

The attraction of OBS profiling is that it can record refracted energy between sources and receivers at very large offsets (tens to hundreds kilometers), well beyond the maximum range of current streamers (up to ~15 km long), and therefore provide useful velocity constraints toward the deepest parts of the oceanic lithosphere. Conversely, the main weakness of OBS profiling is the limited number of deployed instruments, even for the largest and most recent surveys (Kamei et al., 2012; Watremez et al., 2015), which precludes detailed imaging of the shallowest part of the oceanic crust (<600 m). Fortunately, MCS profiling with its much denser source and receiver coverage can, in principle, bridge this shallow-crust resolution gap. Therefore, when available, imaging of oceanic targets can strongly benefit from joint inverse modeling of OBS and MCS refracted data.

#### 3.1. Controlled-Source Seismic Data

In this study, we combined controlled-source seismic data from two existing experiments: (1) the 1999 Axial Seamount air gun-to-OBS survey (West et al., 2001) and (2) the 2002 JdFR MCS survey (Carbotte et al., 2008), both conducted with the *R/V Maurice Ewing*.

The objective of the April 1999 air gun and OBS experiment was to study the large-scale crustal structure of Axial Seamount as a rift volcano and to study the effects of the superposition of the JdFR and Cobb hot spot (West et al., 2001, 2003). The seven-day cruise collected 1,226 km of shot lines over an area spanning Axial Seamount. A total of 5,025 air gun shots were fired at intervals of 60 to 120 s to an array of six OBSs, and 8,210 crustal Pg-phases were used to constrain a 50 km × 50 km tomographic model (West et al., 2001).

In July–August 2002, an extensive MCS survey was carried out over the JdFR and its flanks, between the Cleft and Endeavour segments. For this survey, a 480-channel, 6-km-long Syntron digital streamer with receiver groups spaced at 12.5 m was towed at a nominal depth of 10 m. The source was a tuned, 10-element air gun array with a volume of ~49.2 L (3,005 in<sup>3</sup>), towed at a nominal depth of 7.5 m, with shots fired every 37.5 m along track. A total of 10,265 MCS shots were fired above Axial Seamount, and data were recorded at a sampling rate of 2 ms for 10.24-s-long records. Streamer depth and feathering were derived from 13 depth controlling and 11 compass-enhanced DigiCourse birds, and a tail buoy GPS receiver. The Axial segment was investigated over a 12-day period, and a dense survey comprising 12 two-dimensional MCS profiles was collected over the volcano (Figure 1). Over Axial Seamount, the spacing between the MCS profiles was typically on the order of ~3.5 km.

#### 3.2. SOBE Downward Continuation of MCS Data

For deep-sea environments, the reason that refraction arrivals are secondary arrivals on surface MCS data is that water depths are large relative to the target depths beneath the seafloor. For a shot gather recorded at the surface, the shallowest portion of the oceanic crust, that is, the majority of seismic layer 2A forms a “hidden layer” for which no first arrivals are recorded. For an example shot gather 616 from Line 48 (Figure 2a), which covers the summit caldera of the volcano, only refractions turning >800 m beneath the seafloor are first arrivals in the original data. However, by employing a two-step downward continuation process (or redatuming; see Berryhill, 1979), we first simulate moving the receivers in individual shot gathers to the seafloor and then the sources in common receiver gathers. The resulting data set is a synthetic on-bottom experiment (SOBE; Arnulf et al., 2011; Harding et al., 2007) with refractions turning just bsf appearing as

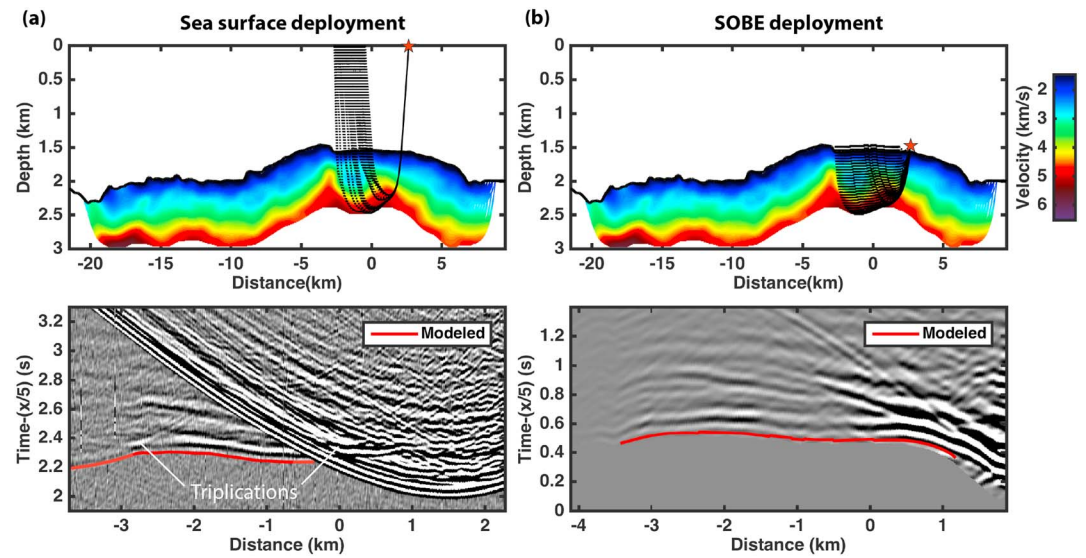


**Figure 2.** Illustration of Synthetic Ocean Bottom Experiment (SOBE) method. (a) Representative shot gather 616 from seismic line 48 recorded on the sea surface with the corresponding arrivals and raypaths. (b) Same shot gather after downward extrapolation to an irregular horizon 75 m above the seafloor. The origin of the distance axis is the intersection between seismic lines 48 and 61 (see Figure 1). The red lines and dashed black lines indicate the first arrival crustal refraction.

first arrivals (Figure 2b). First arrivals are both easier to pick reliably and easier for most tomography algorithms to handle, since by default the ray tracers in these codes compute only first arrival times. We performed the downward continuation using a Kirchhoff implementation in the time domain (Shtivelman & Canning, 1988). The advantage of a Kirchhoff approach is that it can flexibly handle uneven input and output geometries (e.g., Arnulf et al., 2012, 2013; Ghosal et al., 2014; Harding et al., 2016; Henig et al., 2012). On the input side, this allows us to handle unevenly spaced sources and to mitigate the negative effects of streamer feathering. On output, it allows us to downward continue the data to an arbitrary horizon, which can be the seafloor for traveltimes inversion. This output flexibility is particularly valuable in settings such as MORs or submarine volcanoes where there can be steep topographic variations and restricting downward continuation to a horizontal output level would strand some sources and receivers well away from the seafloor.

Minimal processing of the data was done prior to downward extrapolation. Three consistently bad channels were replaced by sinc-function interpolation from the neighboring traces and trace rebalancing was applied, maintaining crucial data continuity between traces. A predictive deconvolution filter was applied to the data to minimize the bubble pulse effect. To minimize edge effects, the first 72 traces and last 12 traces were tapered using a sinusoidal weighting operator. An average water velocity of 1.485 km/s was computed from oceanographic data (temperature, depth, and salinity) and used for data redatuming. A sixth-order Butterworth band-pass filter with corner frequencies of 5 and 20 Hz was applied at both stages of the downward extrapolation to exclude noise and enhance usable frequencies of the refraction data.

### 3.3. Joint OBS-MCS Traveltime Tomography

The traveltimes of first-arrival *P* wave crustal refractions (*P<sub>g</sub>* phases) for the OBSs were taken from West et al. (2001) (Figure 3b). However, to minimize the size of the three-dimensional tomographic model, we trimmed the initial data set by ~50%, keeping only 3,962 OBS *P<sub>g</sub>*-phases that were near the 12 MCS lines (i.e., within the thick black box in Figure 1). This data trimming removed predominantly large offsets shot-receiver pairs resulting in a loss of coverage at depths >4.5 km. The number of rays turning in shallower portions of the volcano remained nearly unchanged, offering similar velocity constraints at depths <4.5 km. A pick uncertainty of 30–80 ms was assigned to all OBS phases, depending on the offset, lower than the final 89 ms root-mean-square (RMS) traveltimes misfit observed in the final tomographic inversion of West et al. (2001). By doing so, we slightly increased the relative importance of OBS phases in the joint inversion.

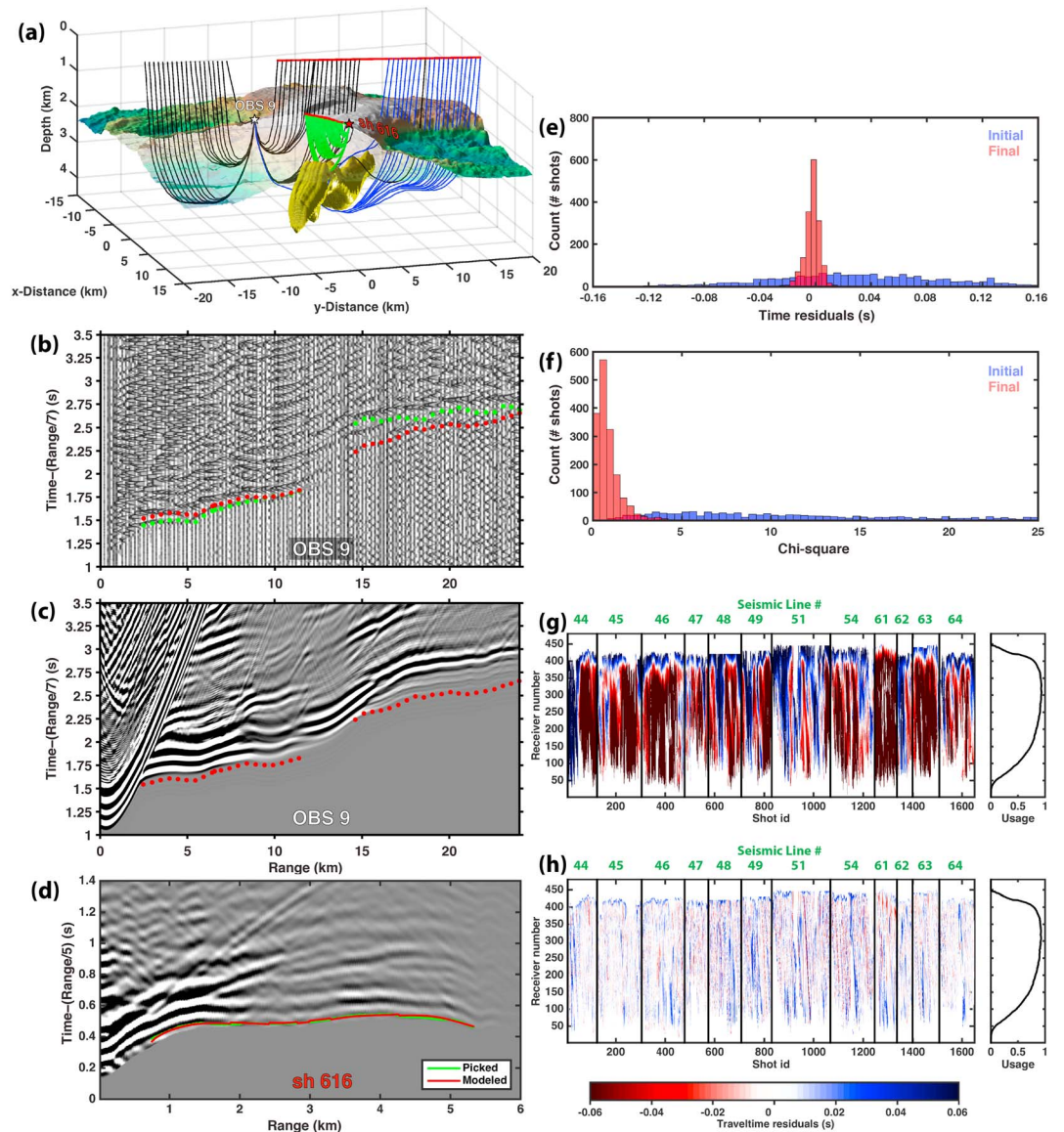


**Figure 3.** Illustration of the data fit and traveltime residuals. (a) 3-D perspective view of all refracted arrivals from SOBE shot gather 616 (light green lines), and refracted arrivals from receiver gather OBS 9 (see West et al., 2001). The black and blue lines mark raypaths refracting above and within or below the main magma reservoir (yellow volume). The red lines highlight all offsets showed in seismic-gather figures (b–d). (b) Measured and (c) synthetic receiver gathers for OBS 9. Observed picks (green dots) for all air gun shots to OBSs are the same as West et al. (2001). (d) SOBE shot gather 616 from seismic line 48. The green lines and green dots mark the observed traveltimes. The red lines and red dots mark the modeled traveltimes using our final 3-D tomographic structure. Distribution of the (e) traveltime residuals and (f) of chi-square for the starting (blue bars) and final (red bars) 3-D models. Residual traveltimes for all 469,891 SOBE pairs, predicted by the (g) initial and (h) final 3-D velocity models displayed as a function of shot number and source-receiver number. Receiver 1 is at 6 km and Receiver 480 at 0.0125 km offset.

Up to ~4.93 million source-receiver pairs were recorded during the 2002 *R/V M. Ewing* MCS survey over Axial Seamount. To optimize the trade-off between spatial resolution of the tomographic model and computational cost associated with picking and inverting more arrivals, our picking strategy was set to select at least one shot falling within the first Fresnel zone at the seafloor (~200 m). Traveltimes of MCS first arrival *P* wave refractions were thus picked along each seismic line, for every fifth SOBE shot gather with full fold coverage (480 traces), representing a total of 1,646 shots, or ~16% of the available shots. Overall, the SOBE shot gathers exhibit a clear and continuous first refracted arrival with high signal-to-noise ratio (Figure 3d) and picking was

possible over a wide range of offsets (Figures 3d and 3g and 3h). To speed up and increase the accuracy and consistency of picking, we used a semiautomatic tool that combined waveform cross-correlation and cluster analysis (Sigloch & Nolet, 2006). Ultimately, 469,891 SOBE source-receiver pairs (~9.5% of all available MCS pairs) were picked (Figures 3g and 3h) and we assigned a picking uncertainty of 12 ms to all SOBE phases, as suggested by the results of Arnulf, Harding, Kent, Singh, et al. (2014) for a similar setting.

As a starting point, an initial 3-D velocity volume was created from a 1-D velocity model attached beneath a 2-D seafloor. The input 1-D velocity structure was a smooth average of the 2-D velocity model of Arnulf, Harding, Kent, Carbotte, et al. (2014) for the upper ~1.2 km of crust and the 3-D velocity model of West et al. (2001) below that horizon. The velocity volume was centered at  $-129^{\circ}59'34.98''\text{W}$ ,  $45^{\circ}55'04.51''\text{N}$ , oriented  $12.9^{\circ}$  from north, and it was 40 km long by 30 km wide by 9 km deep, discretized on a 100 m (horizontal) by 50 m (vertical) rectangular grid.

We then performed 3-D linearized tomographic inversions of the combined 473,853 crustal OBS and SOBE Pg-phases following the methodology of Arnulf, Harding, Kent, Singh, et al. (2014), specific to SOBE MCS data, which was adapted from the Van Avendonk et al. (2004) approach for OBS data. The forward model was calculated using a shortest path method (Moser, 1991) with additional corrections to reduce traveltimes errors associated with the discretization of the seafloor bathymetry. The inversion sought to obtain the smoothest velocity model that fits the data within the pick uncertainties. Models were iteratively updated by minimizing a least squares cost function that penalizes a combination of data misfit and model roughness. We chose a roughness operator that penalized the first and second derivatives (gradient and curvature) of the velocity structure. Horizontal derivatives were given a weight 4 times larger than vertical derivatives to account for the fact that the final seismic velocity structure is expected to be rougher in the vertical direction. The goodness of the fit between observed (picked,  $T_{\text{obs}}$ ) and synthetically calculated ( $T_{\text{syn}}$ ) traveltimes was measured by the  $\chi^2$  value:

$$\chi^2 = \frac{1}{N} \sum_{i=1}^N \frac{(T_{\text{obs},i} - T_{\text{syn},i})^2}{\sigma_{\text{err},i}},$$

where  $\sigma_{\text{err}}$  is a pick uncertainty and  $N$  is the total number of picks. At each iteration, we tracked the overall  $\chi^2$  value (traveltimes fit), as well as the regional distribution of misfit across the entire data set (Figures 3e–3h).

We treated all picked arrivals as first arrivals, and the subsurface velocity volume was composed of a single crustal layer. We carried out 12 initial iterations of the linearized 3-D inversion to constrain the velocity structure above the magma reservoir. Starting at iteration nine, far-offset OBS raypaths largely incompatible with the first-arrival tomographic structure, that is, presenting extreme RMS misfit, were iteratively removed from the observed pick file. Once the velocity structure above the magma reservoir was recovered accurately, we introduced a second crustal layer to the tomographic model to better fit the far-offset secondary arrivals that we initially trimmed out from the pick file. We imposed additional constraints on the shape and physical state of the magma reservoir using high-quality depth-migrated images and velocity models of the reservoir (Arnulf, Harding, Kent, Carbotte, et al., 2014). Migration images along all seven profiles spanning the MMR were used to constrain the 2-D geometry of its roof and floor, and between profiles we used spline interpolation. The shape of the MMR roof was maintained for an additional four iterations. An average velocity of 4 km/s for the MMR was also inferred from previous full waveform inversion modeling (Arnulf, Harding, Kent, Carbotte, et al., 2014) and assigned to all nodes within the reservoir. No smoothing was imposed across the magma chamber roof (the bottom of crustal layer 2). After four additional iterations, the model converged to an average  $\chi^2$  value of 1.01 and all but a few far-offset OBS arrivals were fit within their estimated picking uncertainties (Figures 3e–3h). The reason far-offset picked OBS arrivals from West et al. (2001) (green dots with offsets  $>15$  km; Figure 3b) were not correctly fit is that these arrivals do not correspond to paths of absolute minimum traveltimes. In fact, Figures 3a and 3b show that in the presence of a low-velocity crustal anomaly, paths diffracting above and below the magma reservoir (blue lines on Figure 3a) may exist and travel faster than the body wave phases, as previously described by Wilcock et al. (1995). Full waveform elastic simulation of OBS #9 through our final velocity structure (Figure 3c) further demonstrates that the faster paths may carry very little energy in the high-frequency limit and could be mistakenly ignored in ray theory, although they may transmit substantial energy at finite frequencies (see Wielandt, 1987).

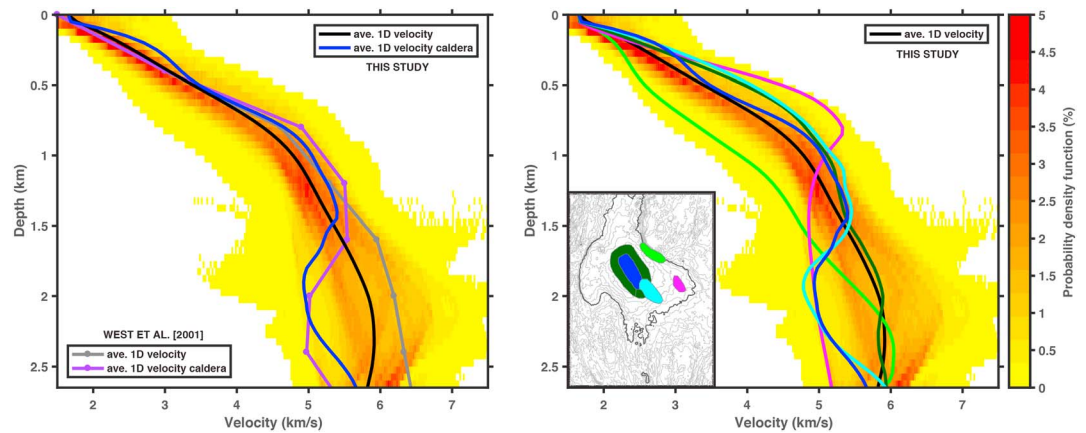


**Figure 4.** Velocity probability distribution for the entire final 3-D velocity volume computed at each depth below the seafloor (colormap). (a) The black line is the average 1-D velocity model through our entire final 3-D velocity structure. The blue line is our average 1-D velocity model computed in the vicinity of the caldera. The gray line is the average 1-D velocity model from West et al. (2001) OBS-tomographic structure. The purple line is the average 1-D velocity model in the vicinity of the caldera in West et al. (2001) OBS-tomographic model. (b) Other colored lines are average 1-D velocity models computed in their respective colored regions (see inset map of Axial Seamount). The blue area covers the summit caldera. The dark-green area marks an  $\sim 2.5$ -km-wide region wrapping around the caldera. The cyan area is located above the MMR, but only to the southeast of the caldera. The pink area is above the central part of the SMR. The light-green area is located above the eastern shoulder of Axial Seamount between the volcano summit and Helium basin. The solid black line on inset map marks the 1.8 km depth contour.

## 4. Tomography Results

The final 3-D tomographic model images the velocity structure beneath Axial Seamount to a depth of  $\sim 4.5$  km. Here we discuss the inversion statistics, the 3-D velocity distribution, and the total velocity gradient magnitude, which highlights changes in the slope of the velocity model. Finally, we estimate values of melt fraction and total melt volume, using a differential effective medium theory.

### 4.1. Inversion Statistics

Overall, the 3-D inversion reduces RMS traveltime residuals from  $\sim 46$  to  $\sim 12$  ms (Figure 3e). Traveltime residuals for the OBS phases alone show a reduction from  $\sim 216$  ms to a final value of  $\sim 90$  ms, comparable to the RMS traveltime misfit attained by West et al. (2001) final tomographic model (89 ms). Similarly, traveltime residuals of the SOBE MCS data (Figures 3g and 3h) uniformly have a significantly lower misfit ( $\sim 11$  ms) in the final velocity structure, which given the dominant scales of heterogeneity along the SOBE lines and spacing of the lines indicate that our preferred model has captured significant portions of the 3-D upper crustal structural variability. Our final velocity structure is compatible not only with existing observed OBS traveltime picks but also with 469,891 additional SOBE MCS traveltime picks and geometrical constraints provided by the depth-migrated images.

### 4.2. Seismic Velocity Structure

Figure 4 presents the  $P$  wave velocity distribution within the final 3-D tomographic model (Arnulf, Harding, & Kent, 2018). Upper crustal velocities range between  $\sim 1.6$  and  $7.5$  km/s and overall seismic velocities increase rapidly within the first  $\sim 900$  m bsf and more gradually afterwards. However, a velocity variability of  $\sim 1.5$  km/s near the seafloor and up to  $\sim 3.5$  km/s at greater depths is observed and required by the inversion to adequately fit the traveltime data. These variations in velocity give clues to the subsurface structure of the volcano.

The largest lateral velocity heterogeneities occur in a region surrounding the horseshoe-shaped caldera and beneath the eastern shoulder of the volcano (Figure 5). At shallow depths, between 0.2 and 0.9 km bsf, an  $\sim 167$  km<sup>2</sup>, ring-shaped region of high-velocity wraps around the caldera walls with maximal extents of  $\sim 10$  and  $\sim 5$  km to the southeast and to the north, respectively (Figures 4b and 5), and minimal extents of  $\sim 2$  km to the northeast and to the southwest. Velocities within this ring are on average 0.5 km/s higher

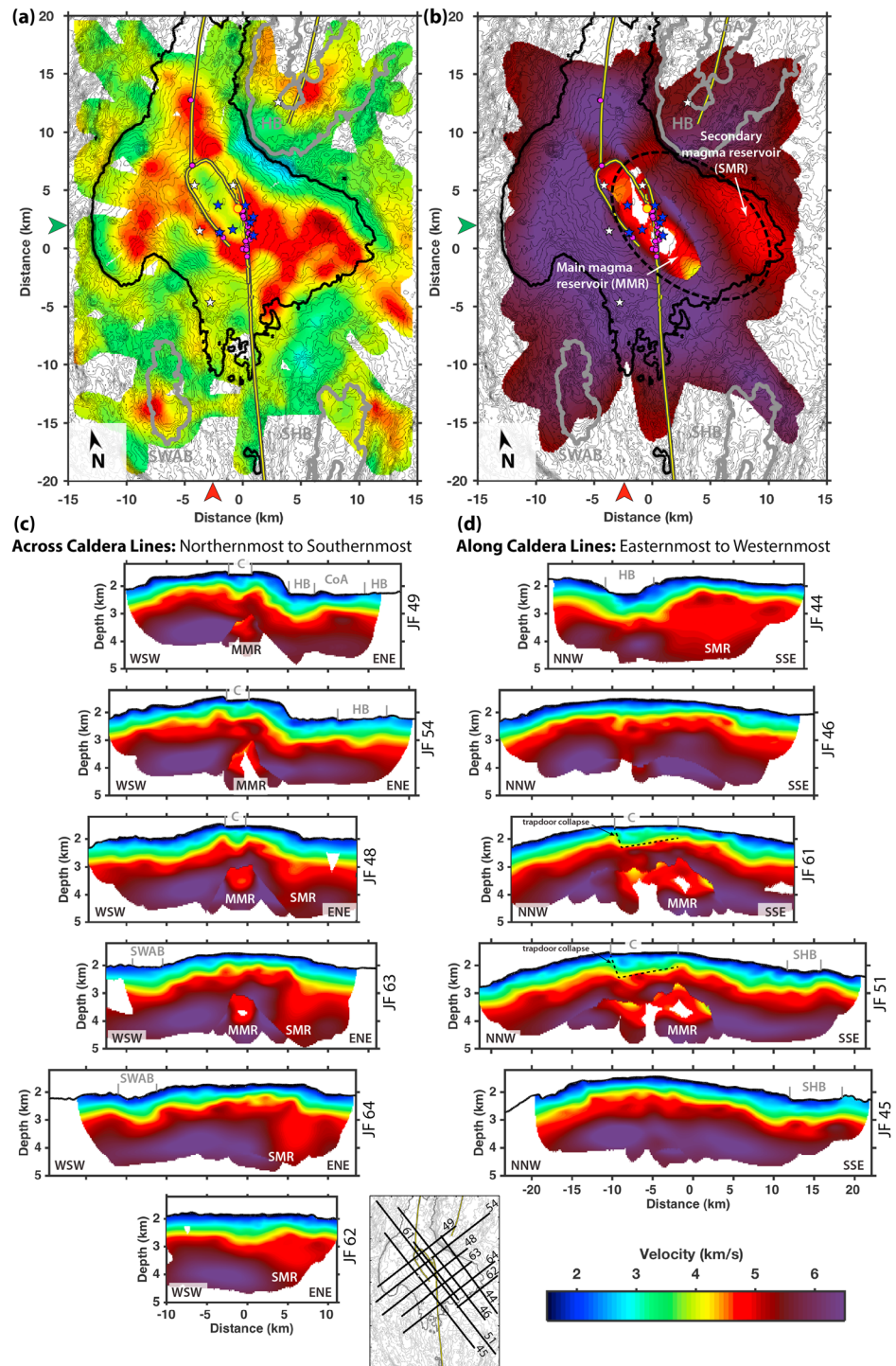


**Figure 5.** Seismic  $P$  wave velocity structure of Axial Seamount (data from Arnulf, Harding, & Kent, 2018). Horizontal velocity slices at depths of (a) 650 m and (b) 2000 m below the seafloor (bsf) with important features of the seafloor (see Figure 1). The solid black line marks the 1.8 km depth contour. The thin black lines mark 25 m depth contour intervals. Thick gray lines mark the contour of the three different basins surrounding the volcano. The dashed black ellipse marks our estimated contour of the Cobb hot spot plume. The green and red arrows mark the position of vertical velocity slices from Figures 7a and 7b, respectively. (c) Vertical velocity slices along all across-caldera MCS seismic lines, from north to south (top to bottom) JF49, JF51, JF48, JF63, JF64, and JF62. (d) Vertical velocity slices along all along-caldera MCS seismic lines, from east to west (top to bottom) JF44, JF46, JF61, JF51, and JF45. The inset map shows the extent of all seismic lines. Acronyms are main and secondary magma reservoirs (MMR and SMR, respectively), caldera (C), Helium basin (HB), coaxial spreading segment (CoA), southwest Axial basin (SWAB), south Helium basin (SHB).

than those within the caldera with the contrast reaching  $\sim 1.25$  km/s at  $\sim 0.65$  km bsf (Figures 4b and 5a). A separate low-velocity region exists beneath the steep northeast shoulder of the volcano, between the caldera and Helium Basin, and velocities within the first kilometer of crust are  $\sim 1$  km/s slower than average (Figures 4b and 5).

At depths greater than  $\sim 1.1$  km bsf, most of the lateral velocity heterogeneity is concentrated within two NNW-SSE elongated low-velocity regions. The main low-velocity region (or MMR; Figures 4 and 5) underlies the horseshoe-shaped caldera and extends toward the southeastern flank of the volcano,  $\sim 5$  km outside of the throat of the caldera. The outline of this low-velocity region was constrained in the tomographic model using migrated sections (Arnulf, Harding, Kent, Carbotte, et al., 2014). The velocity contrast with the surrounding material is high ( $> 1$  km/s). Velocities within the MMR are as low as  $\sim 3.5$  km/s but are on average 4.5–5 km/s (Figures 4b and 5). As expected by the ray theory approach, velocities within the MMR are largely constrained by rays deflecting around the low-velocity anomaly (Figure 3a). Therefore, it is worth noting that our velocity estimates for the MMR represent maximum velocities. To improve velocity estimates within the MMR and to recover the full extent of the low-velocity anomalies, more elaborated techniques making use of more information from the waveform data would need to be employed (e.g., wave-equation tomography of Wang et al., 2014, or full waveform inversion of Jian et al., 2016). A second low-velocity region (secondary magma reservoir, SMR; Figure 5) lies beneath the eastern shoulder of the volcano. No specific constraint regarding the shape of this low-velocity anomaly was provided during the inversion process due to a lack of migration constraints in this region. The resulting low-velocity region is therefore spatially smoothed and extends between 1 and 2.5 km bsf (Figures 4b and 5) with minimum velocities as low as  $\sim 4.7$  km/s.

#### 4.3. Layer 2A Thickness

Arnulf et al. (2011) and Arnulf, Harding, Kent, Singh, et al. (2014) showed that the combination of a SOBE method and 3-D traveltime tomography enables proper imaging of the high-velocity gradient region at the base of layer 2A. The layer 2A thickness map of Figure 6a represents a smoothed surface corresponding to a velocity gradient of  $\sim 3/s$  and was created from picks on crossing vertical profiles extracted from the tomographic structure (solid blue lines in Figures 6c and 6d). The smoothing filter was a 2-D Gaussian (1.5 km radius) convolved with the average thickness measurement map. The map was built from picks less than 2.75 km from a SOBE line.

Although layer 2A thickness is heterogeneous across the study area, with values ranging from 0.4 to 1.4 km, major variations are well correlated with the dominant central volcanic features and delimit three main domains (Figure 6): a domain of relatively thin layer 2A (0.4 to 0.75 km), which broadly corresponds to the elevated volcano; a domain of slightly thicker layer 2A (0.75 to 0.95 km) located beneath the central caldera; and a third domain, located beneath the shoulders of the volcano, where layer 2A is the thickest ( $> 0.95$  km). Sharp variations in layer 2A thickness occur across the caldera bounding faults with vertical throws of 0.25–0.5 km (Figures 6a and 6c: x-Slice  $-2.5$  km and d: y-Slice 5.25 km). Similar layer 2A thickness variations exist across the eastern and southern shoulders of the volcano (Figures 6a and 6c: x-Slice 5 km and d: y-Slice 5.25 and 11 km). Layer 2A is the thickest ( $> 1$  km) beneath Helium Basin and differs from a relatively thin layer 2A (0.6–0.8 km thick) observed underneath the southernmost tip of Coaxial spreading segment (Figure 6a). Additionally, Figure 6 shows that layer 2A thickness is largest to the north rather than just beneath South Helium Basin and Southwest Axial Basin.

It appears that the thinnest layer 2A region, observed beneath the southeast shoulder of the volcano, is located over a narrow and deep crustal root where West et al. (2003) reported oceanic crust up to 11 km thick (Figure 6b). This deep crustal root was interpreted as a region of focused magma oversupply from the Cobb hot spot, and it overlaps part of the two low-velocity regions previously recognized on Figure 5b (MMR and SMR). The contour of this region characterized by a thick crustal root, low crustal velocities (magma reservoirs), and thin upper layer 2A can be approximated by a  $\sim 120$  km<sup>2</sup> elliptical region centered on the southeast shoulder of Axial Seamount (dashed black ellipse, Figures 6a and 6b).

#### 4.4. Melt Fraction Estimate

The effect of melt on seismic properties depends on the composition and microstructure of melt pockets and crystals (Taylor & Singh, 2002). We used different melt inclusion geometries and orientations to estimate minimum and maximum values of melt fraction and total melt volume, using a differential effective

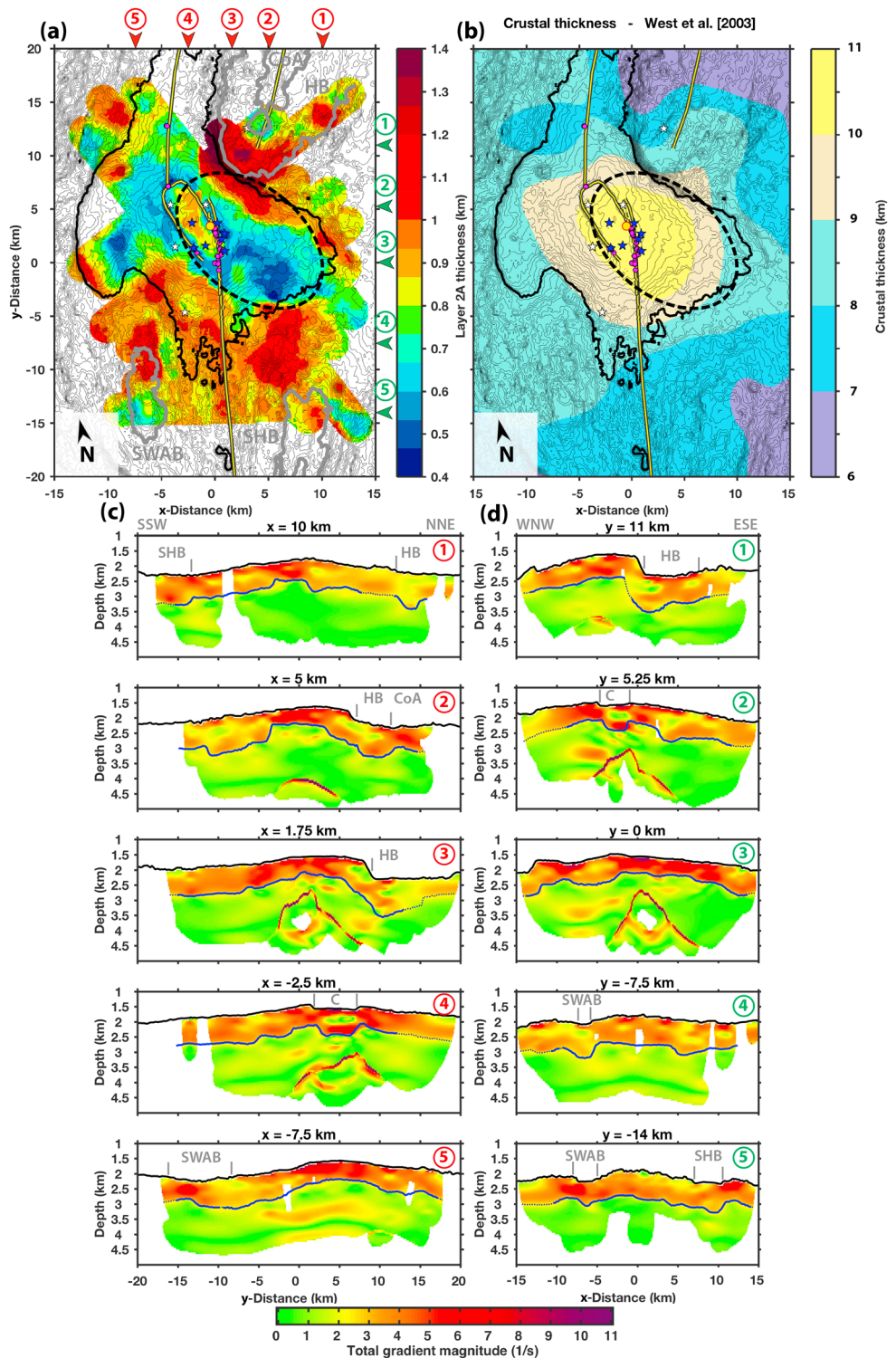


**Figure 6.** (a) Extrusive layer thickness map with important features of the seafloor (see Figure 1). Layer 2A thickness measurements were derived from the total velocity gradient magnitude volume by picking a horizon with gradient value of  $\sim 3$  m/s on all x and y direction slices (c and d). The final layer 2A thickness map is a smoothed average of all x and y direction measurements. The red and green arrows mark the positions of all vertical sections from (c) and (d), respectively. The thick gray lines mark the contour of the three different basins surrounding the volcano. (b) Crustal thickness map from West et al. (2003). The dashed black ellipse marks our estimated location of the Cobb hot spot plume. Vertical cross sections showing the absolute vertical velocity gradient in (c) the x direction and (d) the y direction. The solid and dashed blue lines mark the bottom of layer 2A in all areas within  $\leq 2.5$  km and  $> 2.5$  km of a MCS seismic line, respectively. Acronyms are as in to Figure 5.

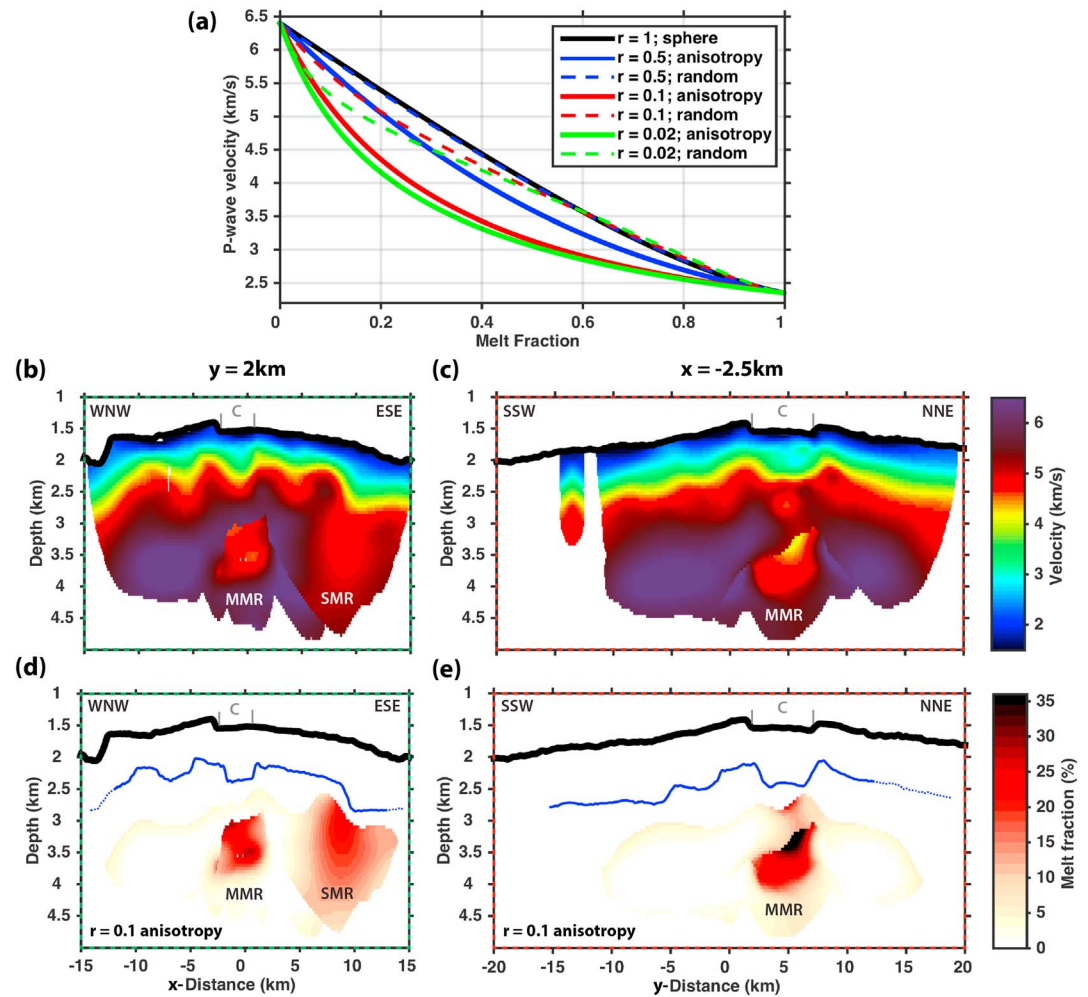


**Figure 7.** Melt fraction estimates using a differential effective medium theory. (a)  $P$  wave velocity variations with melt fraction for inclusions of aspect ratio  $r = 1$  (spherical);  $r = 0.5$ ,  $r = 0.1$ , and  $r = 0.02$  (elliptical). In our modeling, we assumed a two-phase medium consisting of basalt ( $V_p = 6.4$  km/s,  $V_s = 3.5$  km/s, density =  $2,971$  kg/m<sup>3</sup>) and basaltic melt ( $V_p = 2.35$  km/s,  $V_s = 0$  km/s, density =  $2,700$  kg/m<sup>3</sup>). The solid and dashed lines correspond respectively to vertically aligned and randomly aligned elliptical inclusions. Vertical  $P$  wave velocity slices at (b)  $y = 2$  km and (c)  $x = -2.5$  km (the positions are indicated by green and red arrows on Figures 5a and 5b). Melt fraction within layer 2B using a differential effective medium theory (Taylor & Singh, 2002) and vertically aligned elliptical melt inclusions with an aspect ratio  $r = 0.1$  at (d)  $y = 2$  km and (e)  $x = -2.5$  km. The blue lines mark the bottom of layer 2A. Acronyms are as in Figure 5.

medium theory (Berryman et al., 2002; Taylor & Singh, 2002; Figure 7 and Table 2). In our modeling, we assumed a two-phase medium consisting of solid basalt ( $V_p = 6.4$  km/s,  $V_s = 3.5$  km/s, density =  $2,971$  kg/m<sup>3</sup>; Johnston & Christensen, 1997) and basaltic melt ( $V_p = 2.35$  km/s,  $V_s = 0$  km/s, density =  $2,700$  kg/m<sup>3</sup>; Mainprice, 1997). We computed the melt fraction as a function of velocity for a range of aspect ratios  $r = 1$ ,  $0.5$ ,  $0.1$ , and  $0.02$  (the ratio of the short to long axis of a given melt inclusion; Figure 7a). We restricted the computation of the melt fraction to the two main velocity anomalies within layer 2B (beneath the layer 2A high-velocity gradient region) and their surroundings (Figures 7b–7e). Spherical inclusions (aspect ratio 1; Figure 7a: solid black line; Table 2) lead to the largest inferred volume of melt in the system  $\sim 87$  km<sup>3</sup>, with melt fractions up to  $\sim 65\%$ . Randomly oriented elliptical melt inclusions (Figure 7a, dashed lines, and Table 2) yield similar melt fraction estimates for  $P$  wave velocities  $< 4$  km/s, but noticeably lower estimates for  $P$  wave velocities  $> 4$  km/s when aspect ratios are  $< 0.1$ . However, because the  $P$  wave velocity within the two low-velocity regions is on average  $4.5$ – $5$  km/s (Figures 4 and 7), the effect of randomly oriented elliptical melt inclusions is potentially rather significant. The estimated total volume of melt is reduced to  $40.3$ – $83.7$  km<sup>3</sup> if the aspect ratio is between  $0.02$  and  $0.5$ ,

**Table 2**

*Estimated Total Volume of Melt and Maximum Melt Fraction in Axial Seamount's Magmatic System Using a Differential Effective Medium Theory With Several Melt Inclusions*

	Total melt volume (km <sup>3</sup> )	Maximum melt fraction (%)
Spherical inclusion:		
$r = 1$	86.8	65.2
Randomly oriented:		
$r = 0.5$	83.7	65.3
$r = 0.1$	60	65.8
$r = 0.02$	40.3	66.5
Vertically aligned-anisotropy (slow direction):		
$r = 0.5$	62.8	56.3
$r = 0.1$	33.2	42.1
$r = 0.02$	26.7	38.6

although the maximum melt fraction remains unchanged at ~65%. On the other hand, the presence of vertically aligned elliptical melt inclusions would strongly impact our melt fraction estimates, with maximum effect for aspect ratios <0.1 (but very little change for smaller aspect ratios). Fully aligned elliptical inclusions lead to a total volume of melt of 26.7–62.8 km<sup>3</sup> and maximum melt fraction between 39 and 56% (Figure 7a, solid lines, and Table 2).

## 5. Location of Earthquakes With Our New 3-D Velocity Structure and a Grid-Search Algorithm

Wilcock, Tolstoy, et al. (2016) provided the first locations for the earthquakes associated with the 2015 eruption of Axial Seamount using one-dimensional *P* and *S* wave velocity models and the Hypoinverse algorithm. Wilcock, Tolstoy, et al. (2016) also relocated selected events using a double-difference algorithm (hypoDD). The complex velocity

structure near Axial caldera and the limited aperture of the permanent OBS array on the volcano summit means that hypocenter locations are sensitive to the velocity model used. Here we investigate the effect on hypocenter locations of using our 3-D velocity model rather than an average 1-D model.

### 5.1. Data and Methods

We applied a 3-D grid-search algorithm (e.g., Sohn et al., 2004) to the earthquake catalog from Wilcock, Tolstoy, et al. (2016) and Wilcock, Waldhauser, et al. (2016), extending from 22 January to 30 November 2015, with a minimum of 10 arrival times including at least three *S* wave times, for a total of 51,197 events. Theoretical *P* wave traveltime volumes were calculated for each of the seven Cabled Array seismic stations on the summit of Axial to every grid node in our tomographic model using a shortest path ray tracer (Moser, 1991). Theoretical *S* wave traveltime volumes were calculated after applying an empirical  $V_p/V_s$  ratio transfer function to our 3-D *P* wave velocity structure. Our transfer function is a modification of that used by Wilcock, Tolstoy, et al. (2016), which we found reduces the final RMS traveltime residuals.  $V_p/V_s$  changes linearly with *P* wave velocity from 2.2 at  $V_p = 2.0$  km/s to 1.72 at  $V_p = 5.0$  km/s and  $V_p/V_s$  ratio remains constant at 1.72 for  $V_p > 5.0$  km/s.

For each earthquake, we run an exhaustive search through the 3-D structure to identify the grid node with minimum weighted-residual. Discretization was 100 m horizontally and 50 m vertically, identical to our final tomographic structure. The solution was then refined using a 10-m grid centered on this node to find the final hypocentral estimate. For this process we defined the weighted-residual as the sum of the weighted least squares (L2) residuals:

$$\sum_{i=1}^N [W_i (TT_{\text{obs}_i} - TT_{\text{calc}_i})]^2$$

where  $W_i$  is the weight given to each traveltime in the Hypoinverse solution of Wilcock, Tolstoy, et al. (2016) (a value between 0 = worst and 1 = best for *P* wave arrivals, and 0 and 0.33 for *S* wave arrivals) and  $TT_{\text{obs}_i}$  and  $TT_{\text{calc}_i}$  are, respectively, the observed and synthetically calculated traveltimes between the hypocentral location and a given station. However, since  $TT_{\text{obs}_i}$  is unknown in the earthquake location problem, it was estimated from the following equation:

$$TT_{\text{obs}_i} = T_{\text{obs}_i} - T_0,$$

where  $T_{\text{obs}_i}$  is the observed arrival time at a given station and  $T_0$  is the origin time of the seismic event. A value for  $T_0$  was estimated for each grid node using the equation

$$T_0 = \frac{\sum_{i=1}^N W_i (T_{\text{obs}_i} - TT_{\text{calc}_i})}{\sum_{i=1}^N W_i}$$

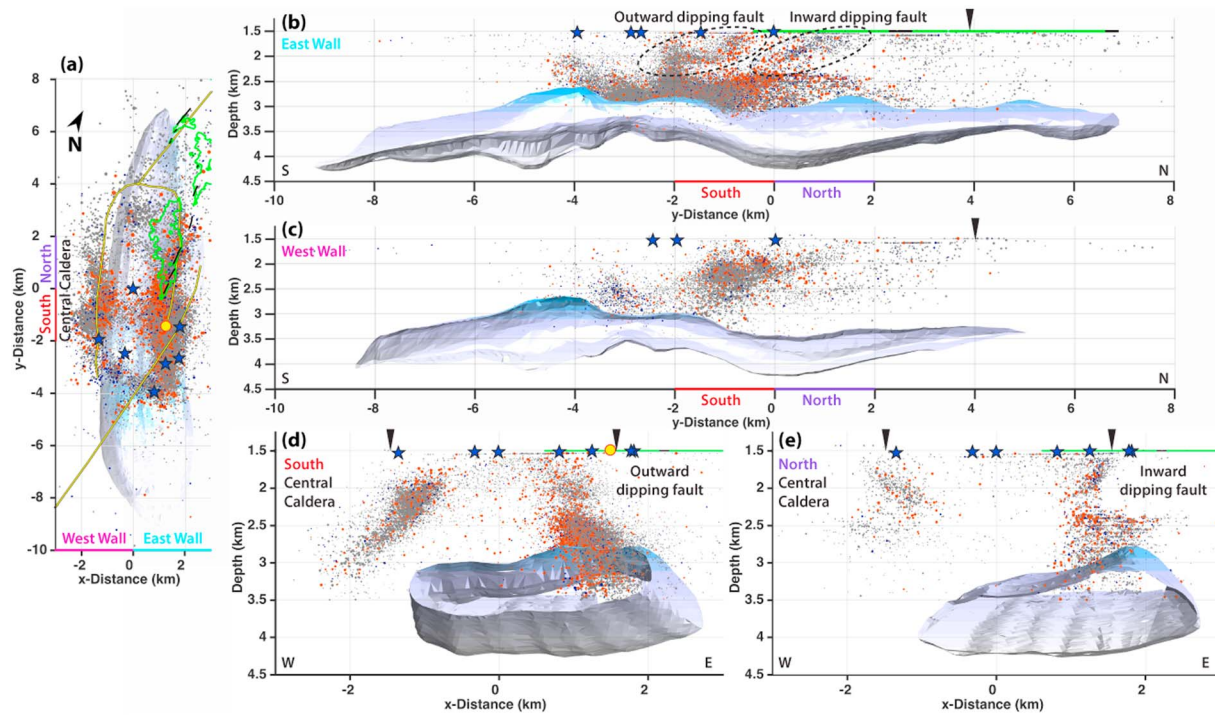


**Figure 8.** Locations of earthquake hypocenters recorded between November 2014 and September 2015 (data from Arnulf, Harding, Kent, & Wilcock, 2018). The grid projection is centered on OOI OBS instrument AXCC1: 45.9547°N/−130.0089°W and rotated −25°N. (a) Map view of the distribution of 51,197 hypocenters located with at least 10 arrival times and a 3-D grid-search algorithm. Seismic events are colored by date (before, on, and after 24 April 2015: gray, orange and blue, respectively). The caldera rim and both rift zones (yellow lines), eruptive fissures (black ticks), lava flows from the 2015 eruption (green contour lines), OOI OBSs (blue stars), and the main magma chamber (shaded colored volume) are also shown. (b) Vertical cross section along the caldera showing all seismic events beneath the east caldera wall ( $x > 0$  km). (c) As in (b) but for all seismic events beneath the west caldera wall ( $x < 0$  km). (d) Vertical cross section across the caldera showing all seismic events beneath the south central caldera ( $y > -2$  km and  $y < 0$  km). (e) As in (d) but for all seismic events beneath the north central caldera ( $y > 0$  km and  $y < 2$  km). The inverted black triangles show the edges of the caldera.

Last, the goodness of the fit between observed and synthetically calculated traveltimes was measured by the RMS residual:

$$RMS = \sqrt{\frac{\sum_{i=1}^N [(TT_{obs_i} - TT_{calc_i})]^2}{N}}$$

The residual vector for our final locations has a RMS misfit of 22.5 ms, which represents an ~12% reduction compared to the Hypoinverse RMS misfit of 25.5 ms from Wilcock, Tolstoy, et al. (2016) using 1-D velocity models.

### 5.2. Three-Dimensional Earthquake Re-location Results

Figure 8 presents our improved hypocenters for the 51,197 local earthquakes in the vicinity of the Axial Seamount MMR originally located by Wilcock, Tolstoy, et al. (2016) using 1-D velocity models (see Figure S1 for comparison). The large-scale features noted by Wilcock, Tolstoy, et al. (2016) are still present: in map view, the earthquake hypocenters define a figure eight pattern beneath the caldera, with the highest concentration of events beneath the east and west caldera walls. However, the distribution of earthquakes differs in a number of details. Beneath the northern end of the caldera, our results show a less diffuse band of shallow seismicity associated with the northern ring of the figure eight distribution (Figure 8a). Additionally, looking at all vertical sections (Figures 8b–8e) we observe that our relocated seismicity is mapped to slightly shallower depths. In across caldera sections, the outward dipping fault zones defined by the seismicity extend from near the seafloor to 3–3.25 km depth and they dip at 42° to 60° (Figure 8d), compared to a maximum

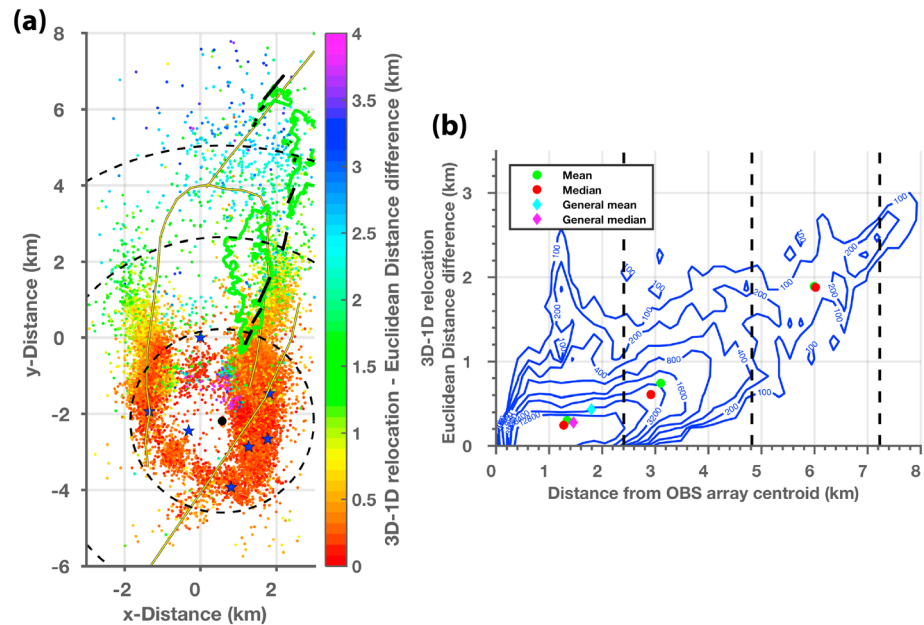


**Figure 9.** Comparison of earthquake location results using our 3-D grid-search method (data from Arnulf, Harding, Kent, & Wilcock, 2018) versus the 1-D approach from Wilcock, Tolstoy, et al. (2016) (data from Wilcock, Tolstoy, et al., 2016). (a) Map projection of the best 26,574 relocated hypocenters, using Wilcock, Tolstoy, et al. (2016) positions, with colors highlighting the absolute Euclidean distance between hypocentral estimates (3-D versus 1-D) for a given event. A black filled circle ( $x = 0.57$  km and  $y = -2.1878$  km) marks the location of the OOI OBS array centroid. The dashed black circles are centered on the OBS array centroid with radius of 2.4, 4.8, and 7.2 km. All other features are as in Figure 9. (b) Density plot showing the Euclidean distance difference between both 1-D and 3-D as a function of the distance from the 2-D OBS array centroid. The dashed black lines correspond to the dashed black circles from (a).

depth of 3.5 km and dips of  $52^\circ$  to  $70^\circ$  in Wilcock, Tolstoy, et al. (2016) (see Figure S1) and dips of  $67^\circ \pm 4^\circ$  in Levy et al. (2018). Additionally, beneath the northern half of the caldera, our revised locations reveal a new set of conjugate inward dipping faults extending from the seafloor to  $\sim 2.25$  km depth and dipping at  $40^\circ$  to  $47^\circ$  (Figure 8e). These two inward dipping bands of seismicity were absent in previous location estimates (i.e., Wilcock, Tolstoy, et al., 2016 and Levy et al., 2018) and are the result of using a 3-D velocity structure in our relocation algorithm. In along caldera sections, our seismicity distribution beneath the east and west walls of the caldera is spatially complex and differs from the mostly conic distribution observed by Wilcock, Tolstoy, et al. (2016) (see Figures S1b and S1c). Beneath the east wall (Figure 8b), a large number of hypocenters form an  $\sim 6$  km-long band of high-seismicity located between  $\sim 2.5$  km and 3 km depth. In addition, two distinct branches of focused seismicity connect the top of the high-seismicity band to the seafloor along southward dipping zones and correspond to the inward and outward dipping faults recognized in across caldera sections (Figures 8d and 8e). Beneath the west wall (Figure 8c), most hypocenters are located in the central caldera and form a broad region of seismicity that is inclined to the south. North of this region, two diffuse bands of seismicity form the inward dipping fault zone recognized on cross caldera sections (Figure 8e).

Figure 9 shows the offsets between the revised locations and the HypoDD locations from Wilcock, Tolstoy, et al. (2016). We show a map projection of the best 26,574 hypocenters from Wilcock, Tolstoy, et al. (2016) with colors highlighting the absolute distance between hypocentral estimates (3-D versus 1-D models) for a given event. To first order, the difference in locations is a function of the distance from the OBS array centroid (black dot in Figure 9a). The mean and median difference in hypocentral location for all events situated within 2.4 km of the OBS array centroid (inner black dashed circle in Figure 9a) are 300 and 245 m, respectively (Figure 9b). These parameters increase rapidly with distance from the OBS array centroid, reaching 740 and 600 m, and 1,890 and 1,880 m, for all events located within 2.4–4.8 km and 4.8–7.2 km of the network centroid, respectively (Figure 9b). Therefore, the benefit of using a 3-D velocity model for earthquake relocations is most pronounced away from the OBS array centroid.

## 6. Discussion

### 6.1. Comparison With an Earlier OBS-Tomography Experiment

The integration of traveltimes arrivals from OBS and SOBE data with a priori structural constraints derived from depth-migrated images reveals the 3-D characteristics of Axial Seamount's internal structure with a level of detail unobtainable for the individual data sets.

West et al. (2001, 2003) analyzed the tomographic data from the 1999 Axial Seamount air gun and OBSs survey. Their velocity field was parameterized on an irregular tetrahedral grid, with variable horizontal node spacing of at best  $2 \text{ km} \times 2 \text{ km}$  and vertical spacing of at best 0.4 km. The velocity grid was vertically sheared to conform to the bathymetry. *P* wave velocities at the seafloor and at 0.4 km bsf were fixed during the inversion with values of 1.5 and 3 km/s, respectively. Therefore, velocity updates were calculated only at depths greater than 0.8 km bsf, as demonstrated by all the 1-D vertical profiles extracted from their velocity cube (Figure S2, dashed gray lines).

Figure 10 compares the OBS-tomographic model of West et al. (2001) with our final, joint SOBE-OBS, tomographic inversion. To illustrate the resolution gain of the joint inversion approach, we resampled the West et al. (2001) OBS-model on two  $0.1 \text{ km}$  (horizontal) by  $0.05 \text{ km}$  (vertical) rectangular grids using different interpolation operators: (1) a nearest-neighbor interpolation function that reflects the discretization of their inverted velocity structure (top panels in Figures 10b and 10c) and (2) a linear interpolation function similar to West et al. (2001) (middle panels in Figures 10b and 10c). Examining the differences between the two resampled OBS models (Figure 10), there are several important observations that can be made. First, in the OBS-only model, 3-D velocity heterogeneities of a given target are often described by a limited number of grid nodes and linear interpolation is commonly used to densify the velocity model prior to ray tracing or illustration (West et al., 2001). However, Miyazawa and Kato (2004) raised concerns about the use of linear interpolation functions, which do not retain the reciprocal relationship between velocity and slowness (traveltimes) fields. Second, because linear interpolation acts as a low-pass filter, smoothing out velocity values within the model space, the resulting reinterpolated velocity field can give a false sense of structural resolution in regions poorly constrained by the inversion, such as the upper crust (see fixed velocity values within the first two-shallowest nodes beneath the seafloor; Figure 4 and in the top panels in Figures 10b and 10c).

However, we would argue that the fixed shallow velocities used by West et al. (2001) were justified given that the OBS data set does not constrain the upper oceanic crust due to the absence of turning rays from depths  $< 600 \text{ m}$ . It is known from other experiments (e.g., Hussenoeder et al., 2002) that for zero age crust, the top of layer 2A should be  $\sim 2 \text{ km/s}$ . By fixing upper crustal velocities, West et al. (2001) ended up with a more realistic looking upper crust than if they had let the tomographic inversion set those velocities (e.g., Canales et al., 1998; Hooft et al., 2000; Hosford et al., 2001; Seher et al., 2010). This is confirmed by the close similarity between the average upper crustal velocity structure of West et al. (2001) and the one recovered by our joint SOBE-OBS inversion, which does have maximum sensitivity in the upper crust (Figure 4a).

Looking at Figure 10, the broad scale features noted by West et al. (2001) are present in our final tomographic structure, including the low velocities of the MMR, and the high-velocity ring wrapped around the MMR. However, because of the fixed upper crustal velocities in the West et al. (2001) model, all the traveltimes delays generated by the heterogeneous upper crust (subsiding caldera, layer 2A thickness variations; see Figure 4) are mapped to greater depths, leading to inaccurate velocity estimates in the underlying model. The most significant effect is observed beneath the central caldera where a spurious vertical pipe of lower velocity connects the upper crust with the MMR (Figure 10). The inclusion of many more shallowly turning rays in the joint SOBE-OBS inversion in addition to structural constraints derived from migrated reflection profiles leads not only to better vertical resolution in the upper kilometer bsf (Figure 6) but also to improved horizontal and vertical resolution everywhere (e.g., velocity variations associated to the main and SMRs). Last, it should be noted that the SOBE model is, as it should be, compatible with the surface MCS traveltimes (Figure 2a), since the surface data are effectively just a subset of the SOBE data set.

### 6.2. Upper Crustal Magma Distribution

Selected portions of the tomographic volume exhibit unusually low velocities (Figures 4 and 5). At depths of  $\sim 2.6\text{--}4.3 \text{ km}$  below the sea surface ( $\sim 1.1\text{--}2.8 \text{ km}$  bsf), particularly low velocities ( $3.5\text{--}5 \text{ km/s}$ ) are present within two NNW-SSE elongated regions located beneath the center and southeast shoulder of Axial

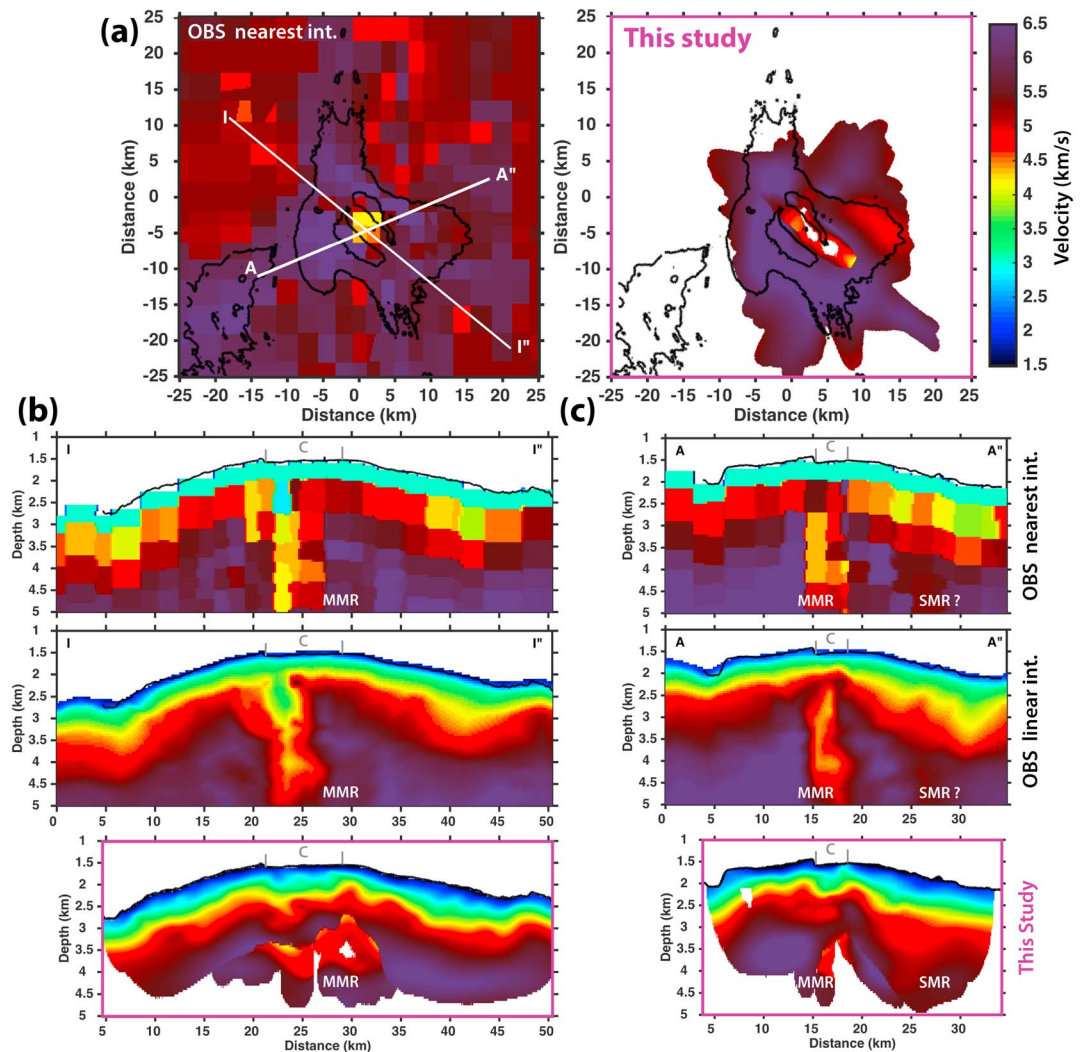


**Figure 10.** Comparison between the air gun to OBS-only  $P$  wave velocity structure from West et al. (2001) (top left) and our joint OBS and SOBE  $P$  wave velocity structure (top right). (a) Horizontal velocity slice at a depth of 2,000 m below the seafloor (bsf). The air gun to OBS-only model (left) was oversampled using a nearest neighbor interpolation operator. The white lines show the location of vertical velocity profiles shown in (b) and (c). The black lines are bathymetry depth contours at 1,525 and 1,800 m. Top and middle plots on (b) and (c) were oversampled using a nearest neighbor and a linear interpolation operator, respectively. Bottom plots in (b) and (c) are from joint OBS and SOBE tomography results. Acronyms are as for Figure 5.

Seamount. Both low-velocity regions are reasonably interpreted to contain significant melt fractions from shallow magma reservoirs (Sigmundsson, 2016), namely, the MMR and SMR (Figure 5). In addition, on the basis of laboratory studies, which show that intergranular basaltic melt is distributed in thin elongated inclusions with an aspect ratio  $r < 0.1$  (Faul et al., 1994), lower and upper bounds for the total volume of melt stored within Axial's magmatic system are  $26.7 \text{ km}^3$  (vertically aligned inclusions with  $r = 0.02$ ) and  $60 \text{ km}^3$  (randomly aligned inclusions with  $r = 0.1$ ) respectively, and the maximum melt fraction is between 38.6 and 65.8% (Table 2). This range reflects uncertainties in the melt distribution but not uncertainties in the velocities. Indeed, it is expected that our tomographic approach underestimates the magnitude of the crustal low-velocity anomalies and thus the volume of melt beneath Axial Seamount. Nevertheless, our estimates of total melt volume are larger than the initial estimates from West et al. (2001) based solely on OBS data ( $5\text{--}21 \text{ km}^3$ ) and more than 2 orders of magnitude larger than the size of recent (1998, 2011, and 2015) magmatic events ( $0.13\text{--}0.3 \text{ km}^3$ ; Table 1), confirming that each eruption only taps a small percentage of the melt in the near-surface magma storage system.

The distribution of melt (volume and depth of the reservoir) present beneath Axial can be put into context by comparing it to some other magmatic systems worldwide. Magma at Axial Seamount is stored within a shallower but larger reservoir than at the 9°N overlapping spreading center on the East Pacific Rise (3.6–5.3 km<sup>3</sup>, depth 1.65–2.2 km; Arnulf, Singh, et al., 2014), Newberry volcano in the Cascade Range (2.5–8 km<sup>3</sup>, depth 3–6 km; Heath et al., 2015), or Soufrière Hills in the lesser Antilles volcanic arc (~4 km<sup>3</sup>, depth 5.5–7.5 km; Paulatto et al., 2012), but the volume of melt stored beneath Axial is much smaller than at the Yellowstone supervolcano magmatic system, where two overlapping magma reservoirs (~900 km<sup>3</sup> each, depth 7+ and 22+ km) with a combined volume of melt of ~1,820 km<sup>3</sup> have been imaged (Huang et al., 2015). In other words, melt storage at Axial Seamount is large compared to typical estimates for plate boundary volcanoes, but relatively modest compared to prominent active hot spot-dominated intraplate volcanoes.

Based only on our 3-D traveltimes tomographic volume, we cannot determine whether or not the two large elongated magma reservoirs are connected and therefore if eruptions at the summit of Axial Seamount can tap the entire magmatic system. However, complementary analysis derived from full waveform inversion and migrated sections has revealed possible magma conduits linking the two reservoirs (Arnulf, Harding, Kent, Carbotte, et al., 2014). We also note that Sohn et al. (1999) relocated posteruption seismicity following the 1998 eruption to a region encompassing both reservoirs. We could interpret this seismicity as evidence of deformation associated with melt displacement between the two reservoirs. However, recent relocations of the posteruption seismicity following the 2015 eruption does not show any particular connection between the MMR and SMR reservoirs (Wilcock, Tolstoy, et al., 2016; Wilcock et al., 2018). To better understand magma accumulation processes within the SMR and magma movement between the two reservoirs, more geophysical instrumentation (i.e., seismometers and geodetic instruments) is needed over the southeast shoulder of Axial Seamount.

### 6.3. Effects of the Cobb Hot Spot on the JdFR

It is of interest to quantify and evaluate the influence of excess magma supply from the Cobb hot spot onto rheological, magmatic, tectonic, and hydrothermal processes along the Axial segment of the JdFR. There is evidence that Axial's unusually large magmatic system, which is the current expression of the Cobb hot spot, provides a large fraction of the melt erupting along the entire ~100-km-long Axial spreading segment (see Figure 1). This evidence includes (1) the southward and northward propagation of dikes and the distribution of recent lava flows along the SRZ and NRZ (Caress et al., 2012; Chadwick et al., 2013, 2016; Dziak & Fox, 1999; Wilcock, Tolstoy, et al., 2016; Wilcock et al., 2018), (2) the presence of two large and shallow elongated magma reservoirs at the center of the segment (Figure 5), (3) the presence of a thick and narrow crustal root beneath the summital magma reservoirs (West et al., 2003), (4) the lack of a crustal axial melt lens reflector on seismic data away from the segment center (Carbotte et al., 2008), and more generally (5) the absence of any sort of mid-crustal, off-axis, or upper mantle melt lens reflectors similar to the ones recognized on nearby JdFR segments (Canales et al., 2009; Nedimovic et al., 2005; Rohr et al., 1988) away from the segment center. However, while the geophysical data suggest the Cobb hot spot strongly influences crustal production, geochemical observations suggest a scenario in which hot spot and MORB magmas mix to varying degrees. Indeed, Chadwick et al. (2005) showed that most hybrid lava samples along the Axial segment are dominated by a MORB-type signature and contain only between 20 and 40% of the Cobb hot spot chemical component.

#### 6.3.1. Relative Contributions of the Cobb Hotspot Plume and JdFR to Crustal Production

Based on the mixing ratios proposed by Chadwick et al. (2005), we consider two end-member models to assess crustal production rates along the Axial segment of the JdFR. For our calculations, we use a 9-km-thick oceanic crust over the central 50 km section of the Axial segment (averaging the excess crustal thickness of West et al., 2003) and a 6-km-thick oceanic crust along the remaining north and south rift zones. For both models, we assume that the total crustal production rate (~1.33 m<sup>3</sup>/s, i.e., vertical section of the Axial segment times spreading rate) is steady state and preserves the present-day crustal thickness (West et al., 2003) and spreading rate along the Axial segment. Our first and second end-member models assume, respectively, that the Cobb hot spot plume is responsible for 20% and 40% of the total crustal production along Axial segment (Figure 11). In these two models, we estimate a crustal production rate (i.e., magma flux) for the Cobb hot spot of ~0.26–0.53 m<sup>3</sup>/s, respectively.

Our revised estimate of the crustal production rate from the Cobb hot spot is slightly smaller than earlier estimates from West et al. (2003) of 0.3 to 0.8 m<sup>3</sup>/s, and comparable or slightly smaller than some other well-

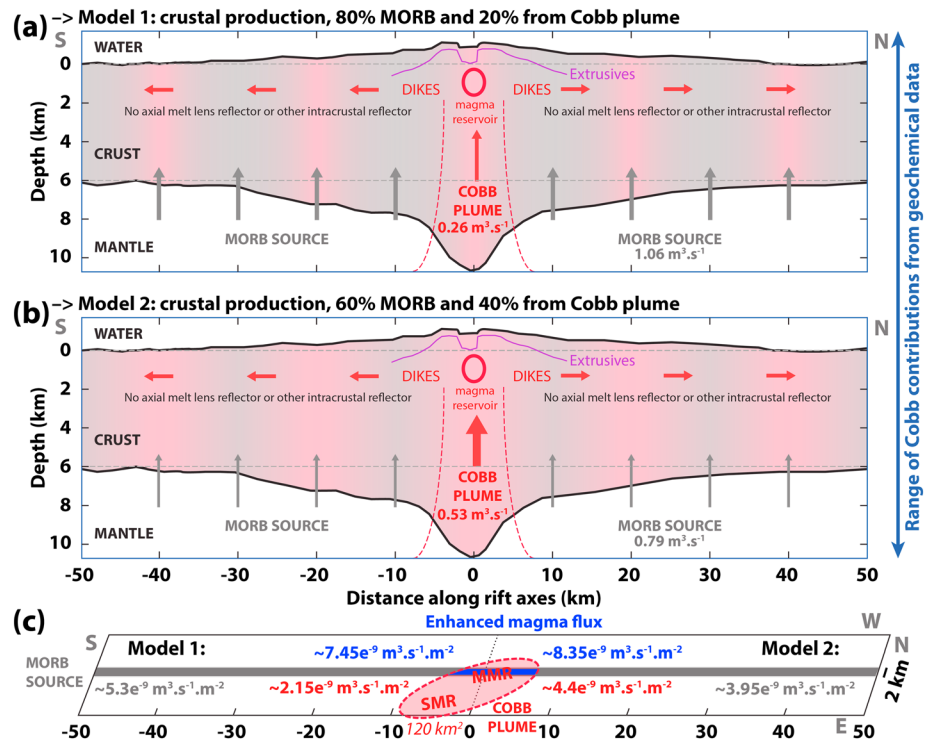


**Figure 11.** (a and b) Vertical schematic models (models 1, and 2 respectively) summarizing the relative contribution of the Cobb hot spot plume and JdFR (MORB source) along the 100-km-long Axial spreading segment, in terms of crustal production rate ( $\text{m}^3/\text{s}$ ). The relative contributions corresponding to both end-member models are derived from geochemical analysis (Chadwick et al., 2005). Crustal thickness is derived from seismic and gravity data (Hooft & Detrick, 1995; West et al., 2003). (c) Schematic section in map view, highlighting the surface across which magma volumetric fluxes ( $\text{m}^3 \cdot \text{s}^{-1} \cdot \text{m}^{-2}$  or  $\text{m}^3/\text{s}$ ) for the MORB source ( $2 \times 100 \text{ km}$  gray rectangle) and for the Cobb plume ( $120 \text{ km}^2$  dashed red ellipse) are computed. Beneath the MMR, the Cobb plume and the MORB source locally overlap leading to enhanced volumetric flux (blue values). Values are for models 1 and 2, to the left and right, respectively.

studied magmatic hot spots worldwide (see White, 1993), such as the Canaries ( $\sim 0.63 \text{ m}^3/\text{s}$ ), Cape Verdes ( $\sim 0.95 \text{ m}^3/\text{s}$ ), or La Reunion ( $\sim 1.27 \text{ m}^3/\text{s}$ ). However, crustal production rate from the Cobb hot spot remains moderate compared to vigorous magmatic hotspots such as Galapagos ( $5.5 \text{ m}^3/\text{s}$ ; Canales et al., 2002), Iceland ( $7 \text{ m}^3/\text{s}$ ; Ito et al., 1996), Hawaii ( $8$  to  $>10 \text{ m}^3/\text{s}$ ; Van Ark & Lin, 2004; Vidal & Bonneville, 2004), Yellowstone ( $9.5 \text{ m}^3/\text{s}$ ; Lowenstern & Hurwitz, 2008), and the Ninety East Ridge ( $2$  to  $15 \text{ m}^3/\text{s}$ ; Sreejith & Krishna, 2015). In addition, knowing that the total volume of recent magmatic events at Axial Seamount is  $0.15\text{--}0.3 \text{ km}^3$ , we can estimate a recurrence interval of 12–24 years between eruptions that would satisfy the total magmatic crustal production rate along Axial segment ( $\sim 1.33 \text{ m}^3/\text{s}$ ). For this calculation, we assumed that eruptive-diking events only form the upper  $\sim 33\%$  of the oceanic crust.

### 6.3.2. Correlation Between the Main Magma Reservoir Depth, Magma Volumetric Flux, and Seafloor Observations

AMC depth depends on the crustal thermal structure of the ridge axis, which is governed by the balance between heat input through magma injection and advective heat removal through hydrothermal circulation (Phipps Morgan & Chen, 1993). Moreover, this dependence is particularly acute within a narrow range of intermediate spreading rates where AMC depth is very sensitive to changes in magma supply. At Axial Seamount, the AMC depth of the top of the MMR ( $1.1\text{--}2.6 \text{ km}$  bsf) is inconsistent with the spreading rate dependence observed at other mid-ocean ridges (Figures 12b and 13). The AMC at Axial is shallower than at any other intermediate-rate spreading segments such as the Southeast Indian Ridge, the Costa Rica Rift, the central East Lau Basin spreading center, the Galapagos spreading center at  $94^\circ\text{W}$ , and all other segments of the JdFR. However, the AMC at Axial Seamount is at comparable depths to fast spreading ridge segments like the Northern East Pacific Rise, the Southern East Pacific Rise, or the hot spot-influenced section of the Galapagos intermediate spreading center at  $92^\circ\text{W}$  (Figure 12b).

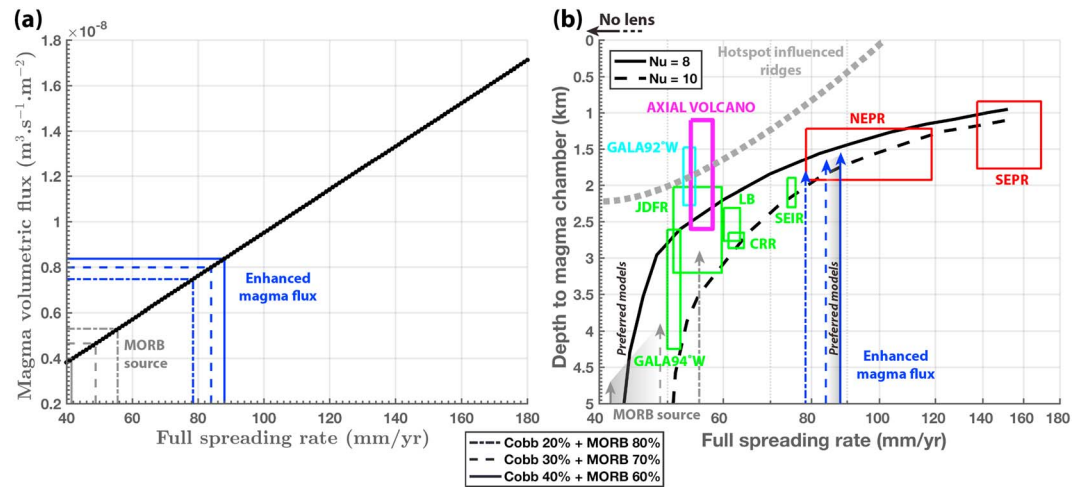


**Figure 12.** (a) Predicted magmatic volumetric flux as a function of spreading rate assuming that melt replenishment occurs within  $\pm 1$  km of the ridge axis (black dotted line). The blue lines are our estimates of enhanced magma volumetric flux and their suggested spreading rate equivalence beneath the summit of Axial Seamount for three different contribution models including the two end-member models from Figure 11. The gray lines are the corresponding magma volumetric flux estimates and suggested spreading rate equivalence for the MORB component. (b) Observed and predicted AMC depth as a function of spreading rate (Chen & Lin, 2004). The solid and dashed lines show numerical results from Chen and Lin (2004) for a reference potential mantle temperature  $T_m = 1350$  °C, crustal thickness  $H_c = 6$  km, and values of the Nusselt number  $Nu$  (the ratio of convective to conductive heat transfer in a hydrothermal convective system) or 8 and 10, respectively. The magenta rectangle shows results from this study at Axial Seamount. Data from other spreading centers are Southern East Pacific Rise (SEPR; e.g., Hussenoeder et al., 1996; Hooft et al., 1997; Tolstoy et al., 1997), Northern East Pacific Rise (NEPR; e.g., Arnulf, Singh, et al., 2014; Carbotte et al., 2013; Harding et al., 1989; Kent et al., 2000), Southeast Indian Ridge (SEIR; Baran et al., 2005), Costa Rica Rift (CRR; Mutter, 1995), central East Lau Basin spreading center (LB; Jacobs et al., 2007), Juan de Fuca Ridge (JdFR; Canales et al., 2005; Carbotte et al., 2008; Van Ark et al., 2007), and the Galapagos spreading center at 94°W (GALA94°W; Blacic et al., 2004). The cyan rectangle corresponds to the Galapagos spreading center at 92°W (GALA92°W; Blacic et al., 2004), another hot spot-influenced spreading segment. The red and green rectangles are for fast and intermediate spreading ridges, respectively. The blue and gray arrows are, respectively, the suggested AMC depth estimates given by our proposed magma volumetric flux at the summit of Axial Seamount as well as along the rest of the Axial segment of the JdFR.

Along intermediate to fast spreading MORs in general and along the JdFR in particular, the interaction between magma injection and hydrothermal circulation shape a narrow crustal magmatic system where melt replenishment occurs within  $\pm 1$  km of the ridge axis (Figure 11c). This is evidenced by the typical across-axis width of AMC reflectors along neighborhood segments of the JdFR (Canales et al., 2005; Van Ark et al., 2007), by the across-axis width of the submelt lens low-velocity region at the Endeavor segment of the JdFR (Arnoux et al., 2017), by the 600 °C thermal isotherm in recent numerical models (Chen & Lin, 2004; MacLennan et al., 2004, 2005), and from chemical, petrological, and geophysical observations at mid-ocean ridges and ophiolite sites (MacLeod & Yaouancq, 2000; Perfit & Chadwick, 1998; Zhang et al., 2014). Similarly, at Axial Seamount, we suggest that melt replenishment associated to the Cobb hot spot plume occurs within an  $\sim 120$  km<sup>2</sup> elliptical region localized beneath the center and southeast shoulder of Axial Seamount (see Figures 5b and 6b), where two large magma reservoirs (MMR and SMR) and a narrow deep crustal root have been imaged. With these assumptions, we can assess lower and upper bounds for the magma volumetric flux ( $\text{m}^3 \cdot \text{s}^{-1} \cdot \text{m}^{-2}$  or m/s) of MORB and Cobb hot spot sources at  $3.95 \times 10^{-9}$  to  $5.3 \times 10^{-9}$  m/s and  $2.15 \times 10^{-9}$  to  $4.4 \times 10^{-9}$  m/s, respectively (Figure 11c). Furthermore, we suggest that the Cobb hot spot plume and MORB source partially overlap directly beneath and just to the southeast of the Axial summit caldera leading to a locally enhanced magma volumetric flux of  $7.45 \times 10^{-9}$  to  $8.35 \times 10^{-9}$  m/s (Figure 11c).

Under the same assumption that melt replenishment at intermediate to fast spreading ridges occurs within  $\pm 1$  km of the ridge axis, one can predict the magma volumetric flux of a given MOR as a function of spreading rate (Figure 12a). If we then compare our estimated value of enhanced magma volumetric flux at the summit of Axial Seamount ( $7.45 \times 10^{-9}$  to  $8.35 \times 10^{-9}$  m/s) with predicted values, we find that Axial's magma supply is locally comparable to MORs with a full spreading rate of 79–89 mm/year, in agreement with the similar

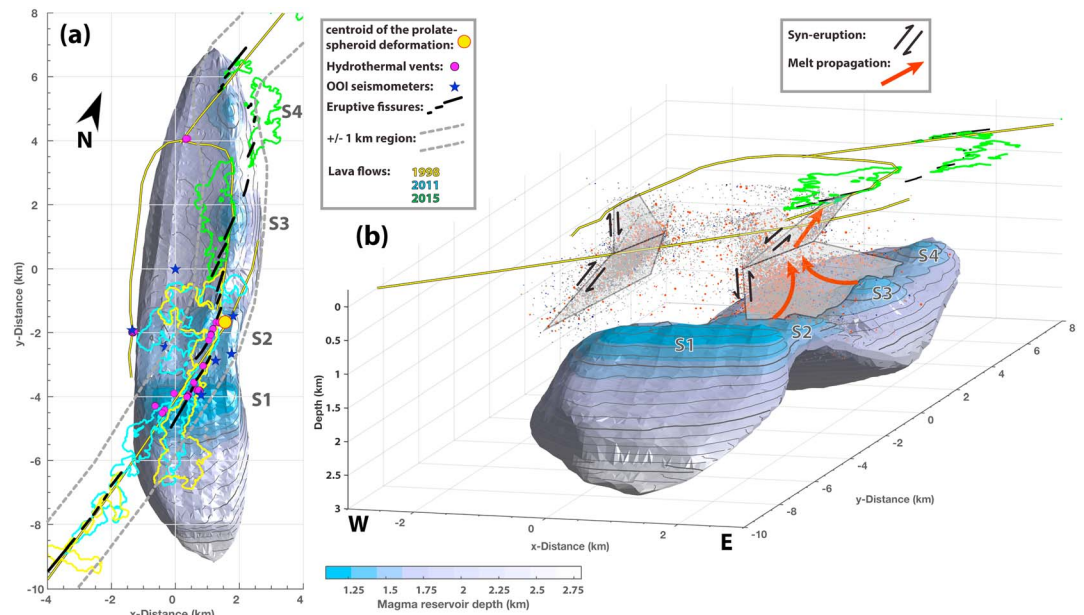


**Figure 13.** Correlation between the main magma chamber geometry and important features from the seafloor (see Figure 1). (a) Map view of the AMC roof topography in depth below the seafloor (bsf). (b) Perspective view of main magma reservoir with seismicity and fault mechanisms associated with the November 2014 to September 2015 Axial Seamount earthquake sequence. S1, S2, S3, and S4 are the four main shallow topographic features from the MMR roof.

AMC depths observed between Axial Seamount and the NEPR (Figure 12b). Therefore, we suggest that (1) enhanced magma supply from the Cobb hot spot is responsible for the presence of a shallow AMC beneath Axial's summit and more importantly (2) that the total magma volumetric flux beneath MORs controls AMC depth. Our models further suggest that Cobb plume contributions of  $\geq 30\%$  to crustal production explain not only the shallow AMC beneath Axial Seamount but possibly the absence of an axial melt lens along the north and south rift zones of Axial segment (Figure 12b). These refined contribution estimates (20–40%) were derived from petrologically derived ratios (Chadwick et al., 2005) and are on par with existing estimates from gravity data ( $\sim 30\%$ ; Hooft & Detrick, 1995). Additionally, Chadwick et al. (2005) showed that the most enriched basalts along Axial segment (up to 60% of the Cobb hot spot component) were recovered at the summit of Axial Seamount, but those basalts were more depleted than any recovered elsewhere on the Cobb-Eickelberg chain (see Figure 1). Chadwick et al. (2005) therefore suggested that Axial Seamount's basalts resulted from the entrainment of MORB mantle in the plume. This observation is also in good agreement with our model where the effect of the Cobb plume on lava composition is expected to be stronger at the center of the segment. Indeed, it is very likely that the Cobb plume changes the thermal isotherms and therefore the magma flow pattern at the base of the lithosphere, entraining more magma at the center of the segment (i.e., into the summit reservoir). Additionally, it is possible that excess magma supply from the Cobb plume not only produces a thickened oceanic crust at the Axial segment but also mitigates the contribution from the MORB source to normal crustal production. The incremental decrease in Cobb hot spot component away from the segment center also suggests that diking events from the summit of Axial along both rift zones are not responsible for the entire segment-scale crustal production. Vertical melt upwelling from a MORB source is therefore expected along the rest of the Axial segment. However, it is likely that the magma volumetric flux from the MOR source is insufficient to provide the appropriate thermal conditions to sustain an axial melt lens. We therefore suggest that melt supply from the MOR component is either episodic or diffuse along both rift zones.

Figure 13a shows the location of known hydrothermal vents and the extent of recent lava flows and eruptive fissures with respect to the MMR roof topography. The topography of the MMR roof reported by Arnulf, Harding, Kent, Carbotte, et al. (2014), with depth variations between 1.1 and 2.6 km bsf, is correlated with these seafloor features. We observe (1) that the MMR is slightly skewed toward the eastern wall of the

caldera and (2) that the eruptive fissures from the 1998, 2011 and 2015 eruptions (black lines on Figure 13a), as well as the deformation source from the 2015 eruption are located within  $\pm 1$  km of the shallowest portions of the MMR ( $< 1.6$  km bsf). These observations suggest that recent eruptive fissures mark the current location of the ridge axis, and they further support our model where enhanced magma supply occurs within a narrow  $\pm 1$  km wide region where both MORB and Cobb hot spot plume sources overlap. Additionally, we observe a good correlation between the areas covered by the different lava flows from the 1998, 2011, and 2015 eruptions and the area and height of shallow topographic features on the MMR roof. Indeed, the two shallowest and largest topographic features on the MMR roof (S1 and S2 highs; Figure 13a) are located beneath the largest flows in the caldera, while the two narrower and slightly deeper topographic highs to the north (S3 and S4 highs; Figure 13a) are located just beneath or near smaller lava flows. There is also a strong correlation between the location and density of hydrothermal vents on the seafloor and the area and magnitude of topographic highs on the MMR roof.

Furthermore, we note a gradual decrease in surface area and a gradual increase in AMC depth for all four topographic highs moving from south to north (S1 to S4; Figure 13). This trend could be explained by the current location of the Cobb hot spot plume, which is skewed to the southeast of the summit caldera. The enhanced magma volumetric flux is expected to be largest near the center of the Cobb hot spot plume, in the vicinity of the S1 topographic high and should decrease toward the northern end of the caldera. This is in good agreement with the MCS-imaged high-melt zone of the magma reservoir beneath the SE caldera (Arnulf, Harding, Kent, Carbotte, et al., 2014), where the hottest and most mafic magma is stored (Clague et al., 2013; Dreyer et al., 2013), and is compatible with the spatial distribution of lava compositions from the 2015 eruption where the most mafic flows were found in the NE caldera (MgO up to 8.3%) while flows on the NRZ were gradually more evolved (MgO down to 7.1%; Chadwick et al., 2016). It is also consistent with the map projection of the deformation model of the 2015 eruption (Nooner & Chadwick, 2016), where a near-vertical conduit with relatively high percentage of melt is present in the core of the MMR, with its top corresponding to the S2 prominence on the roof of the MMR (Figure 13a). However, the vertical extent of the deformation model, 1.75 to 6 km bsf, extends well below the bottom of the MMR ( $\sim 2.1$  km bsf) in the vicinity of the S2 high.

We therefore suggest that the local magma volumetric flux not only exerts control on the AMC depth but could also influence the location of eruptive fissures and the locations of hydrothermal vents and lava flows on the seafloor (Figure 13). This is in good agreement with numerical models, which show that the local stress field around a magma chamber depends on the general loading conditions, on the magma chamber shape, and its depth below the Earth's surface (Acocella, 2007; Gudmundsson, 2012). Indeed, it is very likely that the shallowest and most pressurized portions of the MMR concentrate the highest local extensional stress, producing eruptive fissures from which magmatic dikes can escape and bring magma toward the seafloor. This generally agrees with our new 3-D location estimates of the seismicity associated with the 2015 Axial Seamount eruption, where a system of inward and outward dipping faults connects the shallowest portions of the magma chamber with the seafloor (Figure 13b). It is also worth noting that due to the eastward shift of the MMR relative to the caldera position, the network of faults located beneath the western wall of the caldera is not directly connected with the high-melt zone of the magma reservoir at depth, which likely explains why all recent eruptions at Axial's summit occurred beneath the east wall of the caldera.

#### 6.4. Mechanism for Caldera Formation

Detailed analysis of upper crustal velocities reveals a subsiding caldera floor that appears to be a near perfect trap for the ponding of lava flows (Figures 5 and 6). Layer 2A thickness increases gradually to the northwest reaching  $\sim 900$  m beneath the northern half of the caldera (Figure 6a), indicating a trapdoor mechanism for caldera formation as in some subaerial volcanoes. Analog models of caldera formation suggest two possible causes of trapdoor collapse, preferred magma withdrawal from one side of the caldera (Varga & Smith, 1984) or the existence of an asymmetric or tilted magma chamber (Acocella, 2007; Acocella et al., 2000, 2001; Kennedy et al., 2004; Lipman, 1997). At Axial Seamount, we suggest that trapdoor collapse may be explained by the fact that the SE corner moves up and back down during the eruptive cycle with little elevation change while the NE corner primarily moves down during eruptions with little posteruption uplift. This phenomenon leads to a tilted magma chamber roof, which itself exerts a positive

feedback on trapdoor collapse. This model could be tested by deploying more geodetic instruments in the northern caldera.

Our observations corroborate the experiment in Kennedy et al. (2004) where the greatest caldera subsidence is above the most depressed area of the reservoir. Kennedy et al. (2004) further suggested that trapdoor collapse would occur along predominantly linear faults producing a rectangular caldera, when the magma chamber roof is strongly tilted and its lateral extent is large relative to its depth. This is the case at Axial Seamount where an ~8-km-long by ~3-km-wide rectangular caldera overlies a shallow, 14-km-long magma chamber (MMR) characterized by rough roof topography (Figure 13). Similarly, the fault mechanisms resolved by the new hypocentral location estimates are consistent with focal mechanisms (Levy et al., 2018) and analog experiments (Acocella, 2007), which find that during an eruption the caldera floor moves rapidly downward as a coherent piston between two outward dipping faults (Figures 8d and 13b). Then, continued subsidence of the caldera floor can lead to the formation of inward dipping faults that define the rim of the caldera (Figures 8e and 13b). Interestingly, looking at the distribution of seismicity from the 2015 eruption, we observe that a system of outward dipping faults was imaged by the seismicity in the southern half of the caldera while a system of inward dipping faults was imaged by the seismicity in the northern half (Figure 8). While this pattern might seem unusual, it is also widely recognized that faults can move aseismically. Indeed, it is possible that displacement occurred on both inward and outward dipping faults but that seismicity emanated from only one of the two faults in each given region. This observation should motivate future investigations of seismic time series recorded by the OOI network to study if this pattern is persistent over time. Nevertheless, here we have demonstrated that an accurate 3-D *P* wave velocity model coupled with good seafloor instrumentation has led to the first geophysical evidence of a conjugate network of inward and outward dipping faults being simultaneously seismically active beneath a caldera and that the seismicity pattern could be more precisely located even outside of the station network. To further improve the seismicity distribution beneath Axial Seamount, future research should now focus on improving the shear wave velocity structure within the volcano using a joint hypocenter and shear wave velocity inversion (e.g., Baillard et al., 2017) or seafloor compliance measurements (e.g., Crawford & Webb, 2002). Our work should also help motivate deploying more cabled or temporary seismometers to the north and south of the current OOI-network before the next eruption at Axial Seamount (see Wilcock et al., 2018). A broader network will not only recover more of the distal seismicity which was masked by intense levels of proximal seismicity during the 2015 eruption but would also permit the measurement of a broader range of *P* versus *S* wave phase delays and angular apertures. Additionally, at the few locations where geophysical evidence of caldera collapses along outward dipping faults have been provided (e.g., Bárðarbunga volcano, Gudmundsson et al., 2016; Rabaul caldera, Mori & McKee, 1987), our results should motivate the construction of high resolution 3-D tomographic models with the combined goals of better resolving complex subsurface structures and improving patterns of local seismicity.

Abrupt vertical throws of >300 m beneath the northern caldera wall suggest faulting of a lithologically defined layer 2A, that is, the lava-sheeted dike transition (Figure 6). Our estimate for the volume of extrusive flows deposited within the subsiding caldera is 12.8 km<sup>3</sup>. For this calculation, we included 100% of the volume within the upper layer 2A and 50% of the volume within the ~200-m-thick high-velocity gradient region. This volume is more than 2 orders of magnitude larger than the amount of melt extruded during the most recent eruptions (0.03–0.15 km<sup>3</sup>) and more than 3 orders of magnitude larger than the volume of the inner caldera flow emitted during the 2015 eruption (0.00765 km<sup>3</sup>; Caress et al., 2012; Chadwick et al., 2013, 2016; Clague et al., 2017).

It is worth noting that except for the subsiding caldera, the extrusive thickness over the elevated volcano is relatively thin compared to the surrounding volcano shoulders and north and south rift zones (Figure 6a). This radial increase in extrusive thickness has several important implications for the long-term magmatic history of Axial Seamount. (1) It suggests that the unusually thick (~11 km) oceanic crust observed beneath Axial Seamount is predominantly thickened through diking accretion and gabbro crystallization. (2) It suggests that volcanic flows erupting along the Axial segment are predominantly emitted away from the volcano summit. This second statement is consistent with the observation of more voluminous flows along the NRZ during the 2015 eruption (Chadwick et al., 2016; Clague et al., 2017) and along the south rift zone during the 2011 eruption (Caress et al., 2012). In both cases, distal lava flows were more than 50% of the total volume erupted and reached >100 m thickness.

## 7. Conclusions

In this paper we present a detailed seismic velocity model of the Axial Seamount magmatic system from which we draw the following interpretations and conclusions:

1. We show that the addition of ~470,000 first-arrival traveltimes picks from 12 downward extrapolated MCS seismic lines to an existing OBS-tomographic inversion greatly improves the spatial resolution of the crustal  $P$  wave velocity structure. Furthermore, we show that the introduction of geometrical constraints of the roof of the MMR leads to a final velocity model that is not only in agreement with OBS and MCS observed traveltimes picks, but also with existing high-fidelity, depth-migrated reflectivity images (Arnulf, Harding, Kent, Carbotte, et al., 2014).
2. In the 3-D seismic velocity model, we report two elongated regions of low velocities at depths of 1.1–2.8 km bsf. Each of these two low-velocity regions can be explained by the presence of significant melt fractions from shallow magma reservoirs (MMR and SMR). Using a differential effective medium theory, we suggest that a total of 26–60 km<sup>3</sup> of melt is present within the entire magmatic system, with melt fractions up to 65%.
3. We estimate the crustal production rates for the Cobb hot spot plume and for the Axial segment of the JdFR as 0.26 to 0.53 m<sup>3</sup>/s and 0.79 to 1.06 m<sup>3</sup>/s, respectively. A ~120 km<sup>2</sup> elliptical region roughly outlines both the newly imaged magma reservoirs and the narrow and deep (11 km) crustal root previously reported by West et al. (2003). We suggest that melt replenishment associated to the Cobb hot spot plume is focused within this region from which we estimate the magma volumetric fluxes of the Cobb hot spot plume and of the Axial segment of the JdFR as  $2.15 \times 10^{-9}$  to  $4.4 \times 10^{-9}$  m.s<sup>-1</sup> and  $3.95 \times 10^{-9}$  to  $5.3 \times 10^{-9}$  m/s, respectively. Where the Cobb hot spot plume and the JdFR overlap, magma volumetric flux is locally enhanced ( $7.45 \times 10^{-9}$  to  $8.35 \times 10^{-9}$  m/s).
4. At Axial Seamount, the depth to the top of the MMR (1.1–2.6 km bsf) is inconsistent with the spreading rate dependence observed at other mid-ocean ridges. In fact, the AMC depth at Axial Seamount is similar to observations at the NEPR, a fast spreading segment. However, our estimation of the magma volumetric flux at the summit of Axial Seamount ( $7.45 \times 10^{-9}$  to  $8.35 \times 10^{-9}$  m/s) is comparable to predicted values for MORs with a full spreading rate of 79–89 mm/year. Therefore, we suggest that the combination of the Cobb plume and JdFR magma supply changes the thermal isotherms and therefore the magma flow pattern at the base of the lithosphere, entraining more magma at the center of the segment and causing Axial Seamount to behave like a fast spreading ridge.
5. A strong correlation between the distribution of recent eruptive fissures, lava flows, and hydrothermal vents on the seafloor with the geometry of the MMR roof at depth suggests that the local magma volumetric flux is strongly coupled with shallow magmatic, tectonic, and hydrothermal processes.
6. From the gradient of the velocity structure we also quantify the distribution of extrusive flows over the volcano. We show that while the extrusive section is thick over the entire study area, it is thinnest at the summit of the volcano, where an anomalously thick oceanic crust (11 km) has previously been reported. We therefore suggest that focused and excessive magma supply from the Cobb hot spot predominantly thickens the oceanic crust beneath Axial Seamount through diking accretion and gabbro crystallization.
7. From the extrusive thickness map, we also show that the subsiding caldera floor provides a perfect trap for the ponding of lava flows, supporting a trapdoor mechanism for caldera formation. Additionally, we demonstrate that our three-dimensional model helps improve the location of local seismicity, better resolving a network of conjugate outward and inward dipping faults beneath the caldera walls.

### Acknowledgments

This research was funded through National Science Foundation grants OCE-1357076 and OCE-1536219, and additionally supported by the Institute for Geophysics, part of the Jackson School of Geosciences at the University of Texas at Austin. We thank Maya Tolstoy, Michael West, and William Menke for sharing with us their OBS traveltimes picks. We thank Luc Lavie, Cliff Frohlich, and Nicholas Hayman for insightful comments and discussions. We are also grateful to William Chadwick and three anonymous reviewers, whose comments greatly improved the manuscript. The data for this paper are available at [http://www.marine-geo.org/tools/search/Files.php?data\\_set\\_uid=6864](http://www.marine-geo.org/tools/search/Files.php?data_set_uid=6864). Our final 3-D  $P$  wave velocity tomographic structure (Arnulf, Harding, & Kent, 2018, doi: 10.1594/IEDA/324420) and our hypocentral earthquakes estimates for the 2015 Axial Seamount eruptive sequence (Arnulf, Harding, Kent, & Wilcock, 2018; doi: 10.1594/IEDA/324421) can be found on the Marine Geoscience Data System.

### References

- Acocella, V. (2007). Understanding caldera structure and development: An overview of analogue models compared to natural calderas. *Earth-Science Reviews*, 85(3–4), 125–160. <https://doi.org/10.1016/j.earscirev.2007.08.004>
- Acocella, V., Cifelli, F., & Funicello, R. (2000). Analogue models of collapse calderas and resurgent domes. *Journal of Volcanology and Geothermal Research*, 104(1–4), 81–96. [https://doi.org/10.1016/S0377-0273\(00\)00201-8](https://doi.org/10.1016/S0377-0273(00)00201-8)
- Acocella, V., Cifelli, F., & Funicello, R. (2001). Formation and architecture of nested collapse calderas: Insights from analogue models. *Terra Nova*, 13(1), 58–63. <https://doi.org/10.1046/j.1365-3121.2001.00317.x>
- Arnoux, G. M., Toomey, D. R., Hooft, E. E. E., Wilcock, W. S. D., Morgan, J., Warner, M., & VanderBeek, B. P. (2017). Seismic evidence that black smoker heat flux is influenced by localized magma replenishment and associated increases in crustal permeability. *Geophysical Research Letters*, 44, 1687–1695. <https://doi.org/10.1002/2016GL071990>

- Arnulf, A., Harding, A., & Kent, G. (2018). *Three-dimensional P-wave velocity structure of axial volcano on the Juan de Fuca ridge (investigators: Adrien F. Arnulf, Alistair Harding, Graham Kent)*. Palisades, NY: Interdisciplinary Earth Data Alliance (IEDA). <https://doi.org/10.1594/IEDA/324420>
- Arnulf, A., Harding, A., Kent, G., & Wilcock, W. (2018). *Hypocentral earthquake estimates of seismic events recorded on Axial Seamount from January, 2015 through November, 2015 (investigators: Adrien F. Arnulf, Alistair Harding, Graham Kent, William Wilcock)*. Palisades, NY: Interdisciplinary Earth Data Alliance (IEDA). <https://doi.org/10.1594/IEDA/324421>
- Arnulf, A. F., Harding, A. J., Kent, G. M., Carbotte, S. M., Canales, J. P., & Nedimovic, M. R. (2014). Anatomy of an active submarine volcano. *Geology*, 42(8), 655–658. <https://doi.org/10.1130/G35629.1>
- Arnulf, A. F., Harding, A. J., Kent, G. M., Singh, S. C., & Crawford, W. (2014). Constraints on the shallow velocity structure of the Lucky-Strike Volcano, Mid-Atlantic Ridge, from downward continued multichannel streamer data. *Journal of Geophysical Research*, 119, 1119–1144. <https://doi.org/10.1002/2013JB010500>
- Arnulf, A. F., Harding, A. J., Singh, S. C., Kent, G. M., & Crawford, W. (2012). Fine-scale velocity structure of layer 2A from full waveform inversion of downward continued seismic reflection data at the Lucky Strike Volcano, Mid-Atlantic Ridge. *Geophysical Research Letters*, 39, L08303. <https://doi.org/10.1029/2012GL051064>
- Arnulf, A. F., Harding, A. J., Singh, S. C., Kent, G. M., & Crawford, W. (2013). Nature of upper crust beneath the Lucky Strike volcano using elastic full waveform inversion of streamer data. *Geophysical Journal International*, 196(3), 1471–1491. <https://doi.org/10.1093/gji/ggt461>
- Arnulf, A. F., Singh, S. C., Harding, A. J., Kent, G. M., & Crawford, W. (2011). Strong seismic heterogeneity in layer 2A near hydrothermal vents at the Mid-Atlantic Ridge. *Geophysical Research Letters*, 38, L13320. <https://doi.org/10.1029/2011GL047753>
- Arnulf, A. F., Singh, S. C., & Pye, J. W. (2014). Seismic evidence of a complex multi-lens melt reservoir beneath the 9°N overlapping spreading center at the East Pacific rise. *Geophysical Research Letters*, 41, 6109–6115. <https://doi.org/10.1002/2014GL060859>
- Baillard, C., W. S. D. Wilcock, A. F. Arnulf, M. Tolstoy, & F. Waldhauser (2017). Three-dimensional S-wave tomography under Axial Seamount, *American Geophysical Union, Fall General Assembly*, abstract #V51D-0392.
- Baran, J. M., Cochran, J. R., Carbotte, S. M., & Nedimovic, M. (2005). Variations in upper crustal structure due to variable mantle temperature along the Southeast Indian Ridge. *Geochemistry, Geophysics, Geosystems*, 6, Q11002. <https://doi.org/10.1029/2005GC000943>
- Beachly, M. W., Hooft, E. E. E., Toomey, D. R., & Waite, G. P. (2012). Upper crustal structure of Newberry volcano from P-wave tomography and finite difference waveform modeling. *Journal of Geophysical Research*, 117, B10311. <https://doi.org/10.1029/2012JB009458>
- Berryhill, J. R. (1979). Wave-equation datuming. *Geophysics*, 44(8), 1329–1344. <https://doi.org/10.1190/1.1441010>
- Berryman, J. G., Pride, S. R., & Wang, H. F. (2002). A differential scheme for elastic properties of rocks with dry or saturated cracks. *Geophysical Journal International*, 151(2), 597–611. <https://doi.org/10.1046/j.1365-246X.2002.01801.x>
- Blacic, T. M., Ito, G., Canales, J. P., Detrick, R. S., & Sinton, J. (2004). Constructing the crust along the Galapagos Spreading Center 91.38–95.58W: Correlation of seismic layer 2A with axial magma lens and topographic characteristics. *Journal of Geophysical Research*, 109, B10310. <https://doi.org/10.1029/2004JB003066>
- Calvert, A. J. (1995). Seismic evidence for a magma chamber beneath the slow-spreading Mid-Atlantic Ridge. *Nature*, 377(6548), 410–414. <https://doi.org/10.1038/377410a0>
- Canales, J., Ito, G., Detrick, R., & Sinton, J. (2002). Crustal thickness along the western Galápagos Spreading Center and the compensation of the Galápagos hotspot swell. *Earth and Planetary Science Letters*, 203, 311–327.
- Canales, J. P., Detrick, R. S., Bazin, S., Harding, A. J., & Orcutt, J. A. (1998). Off-axis crustal thickness across and along the East Pacific Rise within the MELT area. *Science*, 280(5367), 1218–1221. <https://doi.org/10.1126/science.280.5367.1218>
- Canales, J. P., Detrick, R. S., Carbotte, S. M., Kent, G. M., Diebold, J. B., Harding, A., et al. (2005). Upper crustal structure and axial topography at intermediate spreading ridges: Seismic constraints from the southern Juan de Fuca Ridge. *Journal of Geophysical Research*, 110, B12104. <https://doi.org/10.1029/2005JB003630>
- Canales, J. P., Nedimovic, M. R., Kent, G. M., Carbotte, S. M., & Detrick, R. S. (2009). Seismic reflection images of a near-axis melt sill within the lower crust at the Juan de Fuca ridge. *Nature*, 460(7251), 89–93. <https://doi.org/10.1038/nature08095>
- Canales, J. P., Tucholke, B. E., Xu, M., Collins, J. A., & DuBois, D. L. (2008). Seismic evidence for large-scale compositional heterogeneity of the oceanic core complexes. *Geochemistry, Geophysics, Geosystems*, 9, Q08002. <https://doi.org/10.1029/2008GC002009>
- Caplan-Auerbach, J., Dziak, R. P., Haxel, J., Bohnenstiehl, D. R., & Garcia, C. (2017). Explosive processes during the 2015 eruption of Axial Seamount, as recorded by seafloor hydrophones. *Geochemistry, Geophysics, Geosystems*, 18, 1761–1774. <https://doi.org/10.1002/2016GC006734>
- Carbotte, S. M., Marjanovic, M., Carton, H., Mutter, J. C., Canales, J. P., Nedimovic, M. R., et al. (2013). Fine-scale segmentation of the crustal magma reservoir beneath the East Pacific Rise. *Nature Geoscience*, 6(10), 866–870. <https://doi.org/10.1038/NNGEO1933>
- Carbotte, S. M., Nedimovic, M. R., Canales, J. P., Kent, G. M., Harding, A. J., & Marjanovic, M. (2008). Variable crustal structure along the Juan de Fuca Ridge: Influence of on-axis hot spots and absolute plate motions. *Geochemistry, Geophysics, Geosystems*, 9, Q08001. <https://doi.org/10.1029/2007GC001922>
- Caress, D. W., Clague, D. A., Paduan, J. B., Martin, J. F., Dreyer, B. M., Chadwick, W. W., et al. (2012). Repeat bathymetric surveys at 1-metre resolution of lava flows erupted at Axial Seamount in April 2011. *Nature Geoscience*, 5(7), 483–488. <https://doi.org/10.1038/ngeo1496>
- Chadwick, W. W., Clague, D. A., Embley, R. W., Perfit, M. R., Butterfield, D. A., Caress, D. W., et al. (2013). The 1998 eruption of Axial Seamount: New insights on submarine lava flow emplacement from high-resolution mapping. *Geochemistry, Geophysics, Geosystems*, 10, 3939–3968. <https://doi.org/10.1002/ggge.20202>
- Chadwick, W. W., Embley, R. W., Milburn, H. B., Meinig, C., & Stapp, M. (1999). Evidence for deformation associated with the 1998 eruption of Axial volcano, Juan de Fuca ridge, from acoustic measurements. *Geophysical Research Letters*, 26, 3441–3444. <https://doi.org/10.1029/1999GL900498>
- Chadwick, W. W., Noonan, S. L., Butterfield, D. A., & Lilley, M. D. (2012). Seafloor deformation and forecasts of the April 2011 eruption at Axial Seamount. *Nature Geoscience*, 5(7), 474–477. <https://doi.org/10.1038/ngeo1464>
- Chadwick, W. W., Paduan, J. B., Clague, D. A., Dreyer, B. M., Merle, S. G., Bobbit, A. M., et al. (2016). Voluminous eruption from a zoned magma body after an increase in supply rate at Axial Seamount. *Geophysical Research Letters*, 43, 12,063–12,070. <https://doi.org/10.1002/2016GL071327>
- Chadwick, W. W., Perfit, M., Ridley, I., Jonasson, I., Kamenov, G., Chadwick, W., et al. (2005). Magmatic effects of the Cobb hot spot on the Juan de Fuca Ridge. *Journal of Geophysical Research*, 110, B03101. <https://doi.org/10.1029/2003JB002767>
- Chen, Y. J., & Lin, J. (2004). High sensitivity of ocean ridge thermal structure to changes in magma supply: The Galapagos Spreading Center. *Earth and Planetary Science Letters*, 221, 263–273.
- Clague, D., Paduan, J., Caress, D., Chadwick, W., Le Saout, M., Dreyer, B., & Portner, R. (2018a). *Interpreted outlines (version 2) as ASCII points of the 2011 lava flows and eruptive fissures at Axial Seamount, Juan de Fuca ridge (investigator David Clague)*. Palisades, NY: Integrated Earth Data Applications (IEDA). <https://doi.org/10.1594/IEDA/324416>

- Clague, D., Paduan, J., Caress, D., Chadwick, W., Le Saout, M., Dreyer, B., & Portner, R. (2018b). *Interpreted outlines (version 2) as ASCII points of the 2015 lava flows and eruptive fissures at Axial Seamount, Juan de Fuca ridge (investigator David Clague)*. Palisades, NY: Integrated Earth Data Applications (IEDA). <https://doi.org/10.1594/IEDA/324418>
- Clague, D. A., Dreyer, B. M., Paduan, J. B., Martin, J. F., Chadwick, W. W., Caress, D. W., et al. (2013). Geologic history of the summit of Axial Seamount, Juan de Fuca Ridge. *Geochemistry, Geophysics, Geosystems*, *14*, 4403–4443. <https://doi.org/10.1002/ggge.20240>
- Clague, D. A., Paduan, J. B., Caress, D. W., Chadwick, W. W. Jr., Saout, M. L., Dreyer, B., & Portner, R. (2017). High-resolution AUV mapping and targeted ROV observations of three historical lava flows at Axial Seamount. *Oceanography*, *30*(4), 82–99. <https://doi.org/10.5670/oceanog.2017.426>
- Coogan, L. A. (2014). Chapter 4.14: The lower oceanic crust. In K. Turekian & H. D. Holland (Eds.) (pp. 497–541). *Treatise on Geochemistry*, New York, NY: Elsevier.
- Crawford, W. C., & Webb, S. C. (2002). Variations in the distribution of magma in the lower crust and at the Moho beneath the East Pacific Rise at 9–10°N. *Earth and Planetary Science Letters*, *203*(1), 117–130. [https://doi.org/10.1016/S0012-821X\(02\)00831-2](https://doi.org/10.1016/S0012-821X(02)00831-2)
- Crisp, J. A. (1984). Rates of magma emplacement and volcanic output. *Journal of Volcanology and Geothermal Research*, *20*(3–4), 177–211. [https://doi.org/10.1016/0377-0273\(84\)90039-8](https://doi.org/10.1016/0377-0273(84)90039-8)
- Delaney, R. D., Johnson, P. H., & Karsten, J. L. (1981). The Juan de Fuca ridge—hot spot—propagating rift system: New tectonic, geochemical, and magnetic data. *Journal of Geophysical Research*, *86*, 11,747–11,750. <https://doi.org/10.1029/JB086iB12p11747>
- Desonie, D. L., & Duncan, R. A. (1990). The Cobb-Eickelberg Seamount chain: hotpot volcanism with mid-ocean ridge basalt affinity. *Journal of Geophysical Research*, *95*, 12,697–12,711. <https://doi.org/10.1029/JB095iB08p12697>
- Detrick, R. S., Mutter, J. C., Buhl, P., & Kim, I. I. (1990). No evidence from multichannel reflection data for a crustal magma chamber in the MARK area on the Mid-Atlantic Ridge. *Nature*, *347*(6288), 61–64. <https://doi.org/10.1038/347061a0>
- Dreyer, B. M., Clague, D. A., & Gill, J. B. (2013). Petrological variability of recent magmatism at Axial Seamount summit, Juan de Fuca Ridge. *Geochemistry, Geophysics, Geosystems*, *14*, 4306–4333. <https://doi.org/10.1002/ggge.20239>
- Dunn, R. A., Toomey, D. R., & Solomon, S. C. (2000). Three-dimensional seismic structure and physical properties of the crust and shallow mantle beneath the East Pacific Rise at 9°30'N. *Journal of Geophysical Research*, *105*, 23,357–23,555. <https://doi.org/10.1029/2000JB900210>
- Dziak, R. P., & Fox, C. G. (1999). The January 1998 earthquake swarm at Axial Volcano, Juan de Fuca Ridge: hydroacoustic evidence of seafloor volcanic activity. *Geophysical Research Letters*, *26*, 3429–3432. <https://doi.org/10.1029/1999GL002332>
- Dziak, R. P., Haxel, J. H., Bohnenstiehl, D. R., Chadwick, W. W. Jr., Nooner, S. L., Fowler, M. J., et al. (2012). Seismic precursors and magma ascent before the April 2011 eruption at Axial Seamount. *Nature Geoscience*, *5*(7), 478–482. <https://doi.org/10.1038/ngeo1490>
- Embley, R. W., Chadwick, W. W., Clague, D., & Stakes, D. (1999). 1998 eruption of Axial volcano: Multibeam anomalies and seafloor observations. *Geophysical Research Letters*, *26*, 3425–3428. <https://doi.org/10.1029/1999GL002328>
- Embley, R. W., Murphy, K. M., & Fox, C. G. (1990). High-resolution studies of the summit of Axial volcano. *Journal of Geophysical Research*, *95*, 12,785–12,812. <https://doi.org/10.1029/JB095iB08p12785>
- Faul, U. H., Toomey, D. R., & Waff, H. S. (1994). Intergranular basaltic melt is distributed in thin, elongated inclusions. *Geophysical Research Letters*, *21*, 29–32. <https://doi.org/10.1029/93GL03051>
- Fox, C. G. (1999). In situ ground deformation measurements from the summit of Axial Volcano during the 1998 volcanic episode. *Geophysical Research Letters*, *26*, 3437–3440. <https://doi.org/10.1029/1999GL900491>
- Ghosal, D., Singh, S. C., & Martin, J. (2014). Shallow subsurface morphotectonics of the NW Sumatra subduction system using an integrated seismic imaging technique. *Geophysical Journal International*, *198*(3), 1818–1831. <https://doi.org/10.1093/gji/ggu182>
- Gudmundsson, A. (2012). Magma chambers: Formation, local stresses, excess pressures, and compartments. *Journal of Volcanology and Geothermal Research*, *237–238*(C), 19–41. <https://doi.org/10.1016/j.jvolgeores.2012.05.015>
- Gudmundsson, M. T., Jónsdóttir, K., Hooper, A., Holohan, E. P., Halldórsson, S. A., Ófeigsson, B. G., et al. (2016). Gradual caldera collapse at Bárðarbunga volcano, Iceland, regulated by lateral magma outflow. *Science*, *353*(6296), 262. <https://doi.org/10.1126/science.aaf8988>
- Harding, A. J., Arnulf, A., & Blackman, D. (2016). Velocity structure near IODP Hole U1309D, Atlantis Massif, from waveform inversion of streamer data and borehole measurements. *Geochemistry, Geophysics, Geosystems*, *17*, 1990–2014. <https://doi.org/10.1002/2016GC006312>
- Harding, A. J., G. M. Kent, D. K. Blackman, S. C. Singh, & J.-P. Cannales (2007). A new method for MCS refraction data analysis of the uppermost section at a Mid-Atlantic Ridge core complex, *Eos Trans. AGU*, *88* (52), Fall Meet. Suppl., Abstract S12A-03.
- Harding, A. J., Orcutt, J. A., Kappus, M. E., Vera, E. E., Mutter, J. C., Buhl, P., et al. (1989). Structure of young oceanic crust at 138N on the East Pacific Rise from expanding spread profiles. *Journal of Geophysical Research*, *94*, 12,163–12,196. <https://doi.org/10.1029/JB094iB09p12163>
- Heath, B. A., Hooft, E. E. E., Toomey, D. R., & Bezada, M. J. (2015). Imaging the magmatic system of Newberry Volcano using joint active source and teleseismic tomography. *Geochemistry, Geophysics, Geosystems*, *16*, 4433–4448. <https://doi.org/10.1002/2015GC006129>
- Henig, A. S., Blackman, D. K., Harding, A. J., Canales, J.-P., & Kent, G. M. (2012). Downward continued multichannel seismic refraction analysis of Atlantis Massif oceanic core complex, 30°N, Mid-Atlantic Ridge. *Geochemistry, Geophysics, Geosystems*, *13*, Q0AG07. <https://doi.org/10.1029/2012GC004059>
- Hooft, E., Detrick, R., Toomey, D., Collins, J., & Lin, J. (2000). Crustal thickness and structure along three contrasting spreading segments of the Mid-Atlantic Ridge, 33.5°–35°N. *Journal of Geophysical Research*, *105*, 8205–8226. <https://doi.org/10.1029/1999JB900442>
- Hooft, E. E. E., & Detrick, R. S. (1995). Relationship between axial morphology, crustal thickness, and mantle temperature along the Juan de Fuca and Gorda Ridges. *Journal of Geophysical Research*, *100*(B11), 22,499–22,508. <https://doi.org/10.1029/95JB02502>
- Hooft, E. E. E., Detrick, R. S., & Kent, G. M. (1997). Seismic structure and indicators of magma budget along the southern East Pacific Rise. *Journal of Geophysical Research*, *102*, 27,319–27,340. <https://doi.org/10.1029/97JB02349>
- Hosford, A., Lin, J., & Detrick, R. S. (2001). Crustal evolution over the last 2 m.y. at the Mid-Atlantic Ridge OH-1 segment, 35°N. *Journal of Geophysical Research*, *106*, 12,269–13,285. <https://doi.org/10.1029/2001JB000235>
- Huang, H. H., Lin, F. C., Schmandt, B., Farrell, J., Smith, R. B., & Tsai, V. C. (2015). The Yellowstone magmatic system from the mantle plume to the upper crust. *Science*, *348*(6236), 773–776. <https://doi.org/10.1126/science.aaa5648>
- Hussenöeder, S. A., Collins, J. A., Kent, G. M., Detrick, R. S., & TERA Group (1996). Seismic analysis of the axial magma chamber reflector along the southern East Pacific Rise from conventional reflection profiling. *Journal of Geophysical Research*, *101*, 22,087–22,105. <https://doi.org/10.1029/96JB01907>
- Hussenöeder, S. A., Detrick, R. S., Kent, G. M., Schouten, H., & Harding, A. J. (2002). Fine-scale seismic structure of young upper crust at 17°20'S on the fast spreading East Pacific Rise. *Journal of Geophysical Research*, *107*(B8), 2158. <https://doi.org/10.1029/2001JB001688>
- Ito, G., Lin, J., & Gable, C. W. (1996). Dynamics of mantle flow and melting at a ridge-centered hotspot: Iceland and the Mid-Atlantic Ridge. *Earth and Planetary Science Letters*, *144*, 53–74.

- Ito, G., Lin, J., & Graham, D. (2003). Observational and theoretical studies of the dynamics of mantle plume-mid-ocean ridge interaction. *Reviews of Geophysics*, 41(4), 1017. <https://doi.org/10.1029/2002RG000117>
- Jacobs, A. M., Harding, A. J., & Kent, G. M. (2007). Axial crustal structure of the Lau back-arc basin from velocity modeling of multichannel seismic data. *Earth and Planetary Science Letters*, 259, 239–255. <https://doi.org/10.1016/j.epsl.2007.04.021>
- Jian, H., Singh, S. C., Chen, Y. J., & Li, J. (2016). Evidence of an axial magma chamber beneath the ultraslow-spreading Southwest Indian Ridge. *Geology*, 45(2), 143–146. <https://doi.org/10.1130/G38356.1>
- Johnson, P. H., & Embley, R. W. (1990). Axial Seamount: An active ridge axis volcano on the central Juan de Fuca ridge. *Journal of Geophysical Research*, 95, 12,689–12,696. <https://doi.org/10.1029/JB095iB08p12689>
- Johnston, J. E., & Christensen, N. I. (1997). Seismic properties of layer 2 basalts. *Geophysical Journal International*, 128(2), 285–300. <https://doi.org/10.1111/j.1365-246X.1997.tb01555.x>
- Kamei, R., Pratt, R. G., & Tsuji, T. (2012). Waveform tomography imaging of a megasplay fault system in the seismogenic Nankai subduction zone. *Earth and Planetary Science Letters*, 317–318, 343–353.
- Kardell, D. A., G. L. Christeson, R. Reece, R. L. Carlson, & A. F. Arnulf (2016). Layer 2A in 70 Ma old oceanic crust: Velocity Analysis in the Western South Atlantic Ocean, *American Geophysical Union, Fall General Assembly*, abstract #T13B-2703.
- Karsten, J. L., & Delaney, J. R. (1989). Hot spot-ridge crest convergence in the northeast Pacific. *Journal of Geophysical Research*, 94, 700–712. <https://doi.org/10.1029/JB094iB01p00700>
- Kelley, D. S., Delaney, J. R., & Juniper, S. K. (2014). Establishing a new era of submarine volcanic observatories: Cabling Axial Seamount and Endeavour Segment of the Juan de Fuca Ridge. *Marine Geology*, 352, 426–450. <https://doi.org/10.1016/j.margeo.2014.03.010>
- Kennedy, B., Stix, J., Vallance, J. W., Lavalley, Y., & Longpre, M.-A. (2004). Controls on caldera structure: Results from analogue sandbox modeling. *Geological Society of America Bulletin*, 116(5), 515–524. <https://doi.org/10.1130/B25228.1>
- Kent, G. M., Singh, S. C., Harding, A. J., Sinha, M. C., Orcutt, J. A., Barton, P. J., et al. (2000). Evidence from three-dimensional seismic reflectivity images for enhanced melt supply beneath mid-ocean-ridge discontinuities. *Nature*, 406(6796), 614–618. <https://doi.org/10.1038/35020543>
- Lees, J. M. (2007). Seismic tomography of magmatic systems. *Journal of Volcanology and Geothermal Research*, 167(1–4), 37–56. <https://doi.org/10.1016/j.jvolgeores.2007.06.008>
- Levy, S., Bohnenstiehl, D. R., Sprinkle, P., Boettcher, M. S., Wilcock, W. S. D., Tolstoy, M., & Waldhauser, F. (2018). Mechanics of fault reactivation before, during, and after the 2015 eruption of Axial Seamount. *Geology*, 46, 447–450. <https://doi.org/10.1130/G39978.1>
- Lipman, P. W. (1997). Subsidence of ash-flow calderas: Relation to caldera size and magma chamber geometry. *Bulletin of Volcanology*, 59(3), 198–218. <https://doi.org/10.1007/s004450050186>
- Lowenstern, J. B., & Hurwitz, S. (2008). Monitoring a supervolcano in repose: Heat and volatile flux at the Yellowstone Caldera. *Elements*, 4(1), 35–40. <https://doi.org/10.2113/GSELEMENTS.4.1.35>
- Maclennan, J., Hulme, T., & Singh, S. C. (2004). Thermal models of oceanic crustal accretion: Linking geophysical, geological and petrological observations. *Geochemistry, Geophysics, Geosystems*, 5, Q02F25. <https://doi.org/10.1029/2003GC000605>
- Maclennan, J., Hulme, T., & Singh, S. C. (2005). Cooling of the lower oceanic crust. *Geology*, 33(5), 357–360. <https://doi.org/10.1130/G21207.1>
- MacLeod, C. J., & Yaouancq, G. (2000). A fossil melt lens in the Oman ophiolite: Implications for magma chamber processes at fast spreading ridges. *Earth and Planetary Science Letters*, 176(3–4), 357–373. [https://doi.org/10.1016/S0012-821X\(00\)00020-0](https://doi.org/10.1016/S0012-821X(00)00020-0)
- Mainprice, D. (1997). Modeling the anisotropic seismic-properties of partially molten rocks found at mid-ocean ridges. *Tectonophysics*, 279(1–4), 161–179. [https://doi.org/10.1016/S0040-1951\(97\)00122-4](https://doi.org/10.1016/S0040-1951(97)00122-4)
- Marjanovic, M., Fuji, N., Singh, S. C., Belahi, T., & Escartin, J. (2017). Seismic signatures of hydrothermal pathways along the East Pacific Rise between 9°16' and 9°56'N. *Journal of Geophysical Research: Solid Earth*, 122, 10,241–10,262. <https://doi.org/10.1002/2017JB015004>
- Miyazawa, M., & Kato, M. (2004). On interpolation functions in traveltimes tomography. *Geophysical Journal International*, 158(1), 169–178. <https://doi.org/10.1111/j.1365-246X.2004.02287.x>
- Morgan, W. J. (1971). Convection plumes in the lower mantle. *Nature*, 230(5288), 42–43. <https://doi.org/10.1038/230042a0>
- Mori, J., & McKee, C. (1987). Outward-dipping ring-fault structure at Rabaul caldera as shown by earthquake locations. *Science*, 235(4785), 193–195. <https://doi.org/10.1126/science.235.4785.193>
- Moser, T. J. (1991). Shortest path calculation of seismic rays. *Geophysics*, 56(1), 59–67. <https://doi.org/10.1190/1.1442958>
- Mutter, C. Z. (1995). Seismic and hydrosweep study of the western Costa Rica rift. *Eos, Transactions American Geophysical Union*, 6, F595.
- Nedimovic, M. R., Carbotte, S. M., Harding, A. J., Detrick, R. S., Canales, J. P., Diebold, J. B., et al. (2005). Frozen magma lenses below the oceanic crust. *Nature*, 436(7054), 1149–1152. <https://doi.org/10.1038/nature03944>
- Nooner, S. L., & Chadwick, W. W. (2009). Volcanic inflation measured in the caldera of Axial Seamount: Implications for magma supply and future eruptions. *Geochemistry, Geophysics, Geosystems*, 10, Q02002. <https://doi.org/10.1029/2008GC002315>
- Nooner, S. L., & Chadwick, W. W. (2016). Inflation-predictable behavior and co-eruption deformation captured by cabled instruments at Axial Seamount. *Science*, 354(6318), 1399–1403. <https://doi.org/10.1126/science.aah4666>
- Paulatto, M., Annen, C., Henstock, T. J., Kiddle, E., Minshull, T. A., Sparks, R. S. J., & Voight, B. (2012). Magma chamber properties from integrated seismic tomography and thermal modeling of Montserrat. *Geochemistry, Geophysics, Geosystems*, 13, Q01014. <https://doi.org/10.1029/2011GC003892>
- Perfit, M. R., & Chadwick, W. W. Jr. (1998). Magmatism at Mid-Ocean Ridges: Constraints from Volcanological and Geochemical Investigations. In W. R. Buck, et al. (Eds.), *Faulting and Magmatism at Mid-Ocean Ridges* (pp. 59–115). Washington, DC: American Geophysical Union. <https://doi.org/10.1029/GM106p0059>
- Phipps Morgan, J., & Chen, Y. J. (1993). Dependence of ridge-axis morphology on magma supply and spreading rate. *Nature*, 364(6439), 706–708. <https://doi.org/10.1038/364706a0>
- Purdy, G. M., Kong, L. S. L., Christeson, G. L., & Solomon, S. C. (1992). Relationship between spreading rate and the seismic structure of mid-ocean ridges. *Nature*, 355(6363), 815–817. <https://doi.org/10.1038/355815a0>
- Rohr, K. M. M., Milkereit, B., & Yorath, C. J. (1988). Asymmetric deep crustal structure across the Juan de Fuca Ridge. *Geology*, 16(6), 533–537. [https://doi.org/10.1130/0091-7613\(1988\)016%3C0533:ADCSAT%3E2.3.CO;2](https://doi.org/10.1130/0091-7613(1988)016%3C0533:ADCSAT%3E2.3.CO;2)
- Seher, T., Singh, S. C., Crawford, W., & Escartin, J. (2010). Upper crustal velocity structure beneath the central Lucky Strike Segment from seismic refraction measurements. *Geochemistry, Geophysics, Geosystems*, 11, Q05001. <https://doi.org/10.1029/2009GC002894>
- Shtivelman, V., & Canning, A. (1988). Datum correction by wave-equation extrapolation. *Geophysics*, 53(10), 1311–1322. <https://doi.org/10.1190/1.1442409>
- Sigloch, K., & Nolet, G. (2006). Measuring finite-frequency body-wave amplitudes and traveltimes. *Geophysical Journal International*, 167(1), 271–287. <https://doi.org/10.1111/j.1365-246X.2006.03116.x>
- Sigmundsson, F. (2016). New insights into magma plumbing along rift systems from detailed observations of eruptive behavior at Axial volcano. *Geophysical Research Letters*, 43, 12,423–12,427. <https://doi.org/10.1002/2016GL071884>

- Singh, S. C., Crawford, W. C., Carton, H., Seher, T., Combiar, V., Cannat, M., et al. (2006). Discovery of a magma chamber and faults beneath a mid-Atlantic ridge hydrothermal field. *Nature*, *442*(7106), 1029–1032. <https://doi.org/10.1038/nature05105>
- Sinton, J. M., & Detrick, R. S. (1992). Mid-ocean ridge magma chambers. *Journal of Geophysical Research*, *97*, 197–216. <https://doi.org/10.1029/91JB02508>
- Sleep, N. H. (1975). Formation of oceanic crust: Some thermal constraints. *Journal of Geophysical Research*, *80*, 4037–4042. <https://doi.org/10.1029/JB080i029p04037>
- Small, C., & Danyushevsky, L. V. (2003). Plate-kinematic explanation for mid-oceanic-ridge depth discontinuities. *Geology*, *31*, 399–402. [https://doi.org/10.1130/0091-7613\(2003\)031%3C0399:PEFMDD%3E2.0.CO;2](https://doi.org/10.1130/0091-7613(2003)031%3C0399:PEFMDD%3E2.0.CO;2)
- Sohn, R. A., Barclay, A. H., & Webb, S. C. (2004). Microearthquake patterns following the 1998 eruption of Axial volcano, Juan de Fuca ridge: Mechanical relaxation and thermal strain. *Journal of Geophysical Research*, *109*, B01101. <https://doi.org/10.1029/2003JB002499>
- Sohn, R. A., Webb, S. C., & Crawford, W. C. (1999). Local seismicity following the 1998 eruption of Axial volcano. *Geophysical Research Letters*, *26*, 3433–3436. <https://doi.org/10.1029/1999GL900505>
- Sreejith, K. M., & Krishna, K. S. (2015). Magma production rate along the Ninetyeast Ridge and its relationship to Indian plate motion and Kerguelen hot spot activity. *Geophysical Research Letters*, *42*, 1105–1112. <https://doi.org/10.1002/2014GL062993>
- Taylor, M., & Singh, S. (2002). Composition and microstructure of magma bodies from effective medium theory. *Geophysical Journal International*, *149*(1), 15–21. <https://doi.org/10.1046/j.1365-246X.2002.01577.x>
- Tolstoy, M., Harding, A. J., & Orcutt, J. A. (1997). Deepening of the axial magma chamber on the southern East Pacific Rise toward the Garrett Fracture Zone. *Journal of Geophysical Research*, *102*, 3097–3108. <https://doi.org/10.1029/96JB03226>
- Toomey, D. R., Purdy, G. M., Solomon, S. C., & Wilcock, W. S. D. (1990). The three-dimensional seismic velocity structure of the East Pacific Rise near latitude 9°30'N. *Nature*, *347*, 639–645.
- Van Ark, E., & Lin, J. (2004). Time variati on in igneous volume flux of the Hawaii-Emperor hot spot seamount chain. *Journal of Geophysical Research*, *109*, B11401. <https://doi.org/10.1029/2003JB002949>
- Van Ark, E. M., Detrick, R. S., Canales, J. P., Carbotte, S. M., Harding, A. J., Kent, G. M., et al. (2007). Seismic structure of the Endeavour Segment, Juan de Fuca Ridge: Correlations with seismicity and hydrothermal activity. *Journal of Geophysical Research*, *112*, B02401. <https://doi.org/10.1029/2005JB004210>
- Van Avendonk, H. J. A., Shillington, D. J., Holbrook, W. S., & Hornbach, M. J. (2004). Inferring crustal structure in the Aleutian island arc from a sparse wide-angle seismic data set. *Geochemistry, Geophysics, Geosystems*, *5*, Q08008. <https://doi.org/10.1029/2003GC000664>
- Varga, R. J., & Smith, B. M. (1984). Evolution of the early Oligocene bonanza caldera, Northeast San Juan volcanic field, Colorado. *Journal of Geophysical Research*, *89*, 8679–8694. <https://doi.org/10.1029/JB089iB10p08679>
- Vidal, V., & Bonneville, A. (2004). Variations of the Hawaiian hot spot activity revealed by variations in the magma production rate. *Journal of Geophysical Research*, *109*, B03104. <https://doi.org/10.1029/2003JB002559>
- Wang, H., Singh, S. C., & Calandra, H. (2014). Integrated inversion using combined wave-equation tomography and full waveform inversion. *Geophysical Journal International*, *198*, 430–446. <https://doi.org/10.1093/gji/ggu138>
- Watremez, L., Lau, K. W. H., Nedimovic, M. R., & Loudon, K. E. (2015). Traveltime tomography of a dense wide-angle profile across Orphan Basin. *Geophysics*, *80*(3), B69–B82. <https://doi.org/10.1190/geo2014-0377.1>
- West, M., Menke, W., & Tolstoy, M. (2003). Focused magma supply at the intersection of the Cobb hotspot and the Juan de Fuca ridge. *Geophysical Research Letters*, *30*(14), 1724. <https://doi.org/10.1029/2003GL017104>
- West, M., Menke, W., Tolstoy, M., Webb, S., & Sohn, R. (2001). Magma storage beneath Axial volcano on the Juan de Fuca mid-ocean ridge. *Nature*, *413*(6858), 833–836. <https://doi.org/10.1038/35101581>
- White, R. (1993). Melt production rates in mantle plumes. *Philosophical Transactions of the Royal Society of London, Series A: Mathematical, Physical and Engineering Sciences*, *342*(1663), 137–153. <https://doi.org/10.1098/rsta.1993.0010>
- Wielandt, E. (1987). On the validity of the ray approximation for interpreting delay times. In G. Nolet (Ed.), *Seismic Tomography* (pp. 85–98). Dordrecht, Holland: Reidel. [https://doi.org/10.1007/978-94-009-3899-1\\_4](https://doi.org/10.1007/978-94-009-3899-1_4)
- Wilcock, W., Dziak, R. P., Tolstoy, M., Chadwick, W. W. Jr., Nooner, S. L., Bohnenstiehl, D. R., et al. (2018). The recent history of Axial Seamount: Geophysical insights into past eruption dynamics with an eye toward enhanced observations of future eruptions. *Oceanography*, *31*(1), 114–123. <https://doi.org/10.5670/oceanog.2018.117>
- Wilcock, W., Tolstoy, M., Waldhauser, F., Garcia, C., Tan, Y. J., Bohnenstiehl, D. R., et al. (2016). The 2015 eruption of Axial Seamount: Seismic constraints on caldera dynamics. *Science*, *354*(6318), 1395–1399. <https://doi.org/10.1126/science.aah5563>
- Wilcock, W., Waldhauser, F., & Tolstoy, M. (2016). *Catalogs of earthquake recorded on Axial Seamount from January, 2015 through November, 2015 (investigators William Wilcock, Maya Tolstoy, Felix Waldhauser)*. Palisades, NY: Interdisciplinary Earth Data Alliance (IEDA). <https://doi.org/10.1594/IEDA/323843>. (Accessed on 14 May 2018)
- Wilcock, W. S. D., Solomon, S. C., Purdy, G. M., & Toomey, D. R. (1995). Seismic attenuation structure of the East Pacific Rise near 9°30'N. *Journal of Geophysical Research*, *100*, 24,147–24,165. <https://doi.org/10.1029/95JB02280>
- Wilson, D. S. (1993). Confidence intervals for motion and deformation of the Juan de Fuca Plate. *Journal of Geophysical Research*, *98*, 16,053–16,071. <https://doi.org/10.1029/93JB01227>
- Zandomenighi, D., Aster, R., Kyle, P., Barclay, A., Chaput, J., & Knox, H. (2013). Internal structure of Erebus volcano, Antarctica imaged by high-resolution active-source seismic tomography and coda interferometry. *Journal of Geophysical Research*, *118*, 1–12. <https://doi.org/10.1002/jgrb.50073>
- Zelt, B. C., Taylor, B., Weiss, J. R., Goodliffe, A. M., Sachpazi, M. H., & Hirn, A. (2004). Streamer tomography velocity models for the Gulf of Corinth and Gulf of Itea, Greece. *Geophysical Journal International*, *159*(1), 333–346. <https://doi.org/10.1111/j.1365-246X.2004.02388.x>
- Zhang, C., Koepke, J., Kirchner, C., Götze, N., & Behrens, H. (2014). Rapid hydrothermal cooling above the axial melt lens at fast-spreading mid-ocean ridge. *Scientific Reports*, *4*(1). <https://doi.org/10.1038/srep06342>